


Review

A Review of CeO₂ Supported Catalysts for CO₂ Reduction to CO through the Reverse Water Gas Shift Reaction

Parisa Ebrahimi, Anand Kumar *  and Majeda Khraisheh 

Department of Chemical Engineering, Qatar University, Doha P.O. Box 2713, Qatar

* Correspondence: akumar@qu.edu.qa

Abstract: The catalytic conversion of CO₂ to CO by the reverse water gas shift (RWGS) reaction followed by well-established synthesis gas conversion technologies could be a practical technique to convert CO₂ to valuable chemicals and fuels in industrial settings. For catalyst developers, prevention of side reactions like methanation, low-temperature activity, and selectivity enhancements for the RWGS reaction are crucial concerns. Cerium oxide (ceria, CeO₂) has received considerable attention in recent years due to its exceptional physical and chemical properties. This study reviews the use of ceria-supported active metal catalysts in RWGS reaction along with discussing some basic and fundamental features of ceria. The RWGS reaction mechanism, reaction kinetics on supported catalysts, as well as the importance of oxygen vacancies are also explored. Besides, recent advances in CeO₂ supported metal catalyst design strategies for increasing CO₂ conversion activity and selectivity towards CO are systematically identified, summarized, and assessed to understand the impacts of physicochemical parameters on catalytic performance such as morphologies, nanosize effects, compositions, promotional abilities, metal-support interactions (MSI) and the role of selected synthesis procedures for forming distinct structural morphologies. This brief review may help with future RWGS catalyst design and optimization.

Keywords: reverse water gas shift reaction; mechanism and kinetics; CeO₂ support; CO₂ conversion; affecting parameters



Citation: Ebrahimi, P.; Kumar, A.; Khraisheh, M. A Review of CeO₂ Supported Catalysts for CO₂ Reduction to CO through the Reverse Water Gas Shift Reaction. *Catalysts* **2022**, *12*, 1101. <https://doi.org/10.3390/catal12101101>

Academic Editor: Anna Kubacka

Received: 27 August 2022

Accepted: 20 September 2022

Published: 23 September 2022

Publisher's Note: MDPI stays neutral with regard to jurisdictional claims in published maps and institutional affiliations.

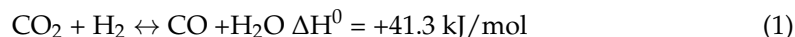


Copyright: © 2022 by the authors. Licensee MDPI, Basel, Switzerland. This article is an open access article distributed under the terms and conditions of the Creative Commons Attribution (CC BY) license (<https://creativecommons.org/licenses/by/4.0/>).

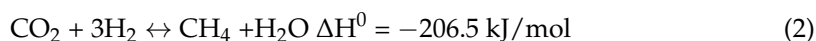
1. Introduction

Carbon dioxide has been identified as the primary anthropogenic greenhouse gas that has resulted in catastrophic climate change and ocean acidification [1,2]. Various approaches have been employed to reduce the amount of CO₂ in the atmosphere. For example, power-to-liquid (PtL) sustainable aviation fuel (SAF) was recently proposed as a long-term and scalable solution to minimize aircraft CO₂ emissions. The procedure turns CO₂ into a synthetic fuel with less sulfur and fewer aromatics, which enhances local air quality and minimizes the effect of aviation at high altitudes [3]. On the other hand, since enormous amounts of low-cost, relatively pure carbon dioxide are available from carbon sequestration and storage facilities, more efforts have been made to utilize CO₂ as an alternative C1 source rather than merely considering it as waste [4]. A unique and appealing alternative to storing CO₂ through sequestration would be recycling the gas into energy-rich compounds via carbon capture, storage and utilization (CCSU) [5,6]. E-fuels, also known as electrofuels or powerfuels, are hydrocarbon fuels produced from hydrogen and CO₂ in which hydrogen is generated from water and electricity through electrolysis and CO₂ is either captured from fossil sources (such as industrial sectors) or the atmosphere [7–9]. E-fuels aim to directly electrify a system without the demand-side adjustments necessary for a direct electrification by substituting fossil fuels with renewable power [7]. However, the CO₂ molecule is a relatively inert and unreactive molecule with a high level of thermodynamic and chemical stability due to its linear chemical structure with double bonds connecting the carbon and oxygen atoms, so converting it to the more

reactive CO is energy-intensive [10]. Among the systems currently available for CO₂ conversion, catalytic conversion to CO, commonly known as the reverse water-gas shift (RWGS) reaction (Equation (1)), is one of the most promising reversible hydrogenation methods that offer a high potential efficiency [11].



RWGS reaction is recognized as an important intermediate stage in a number of key CO₂ hydrogenation reactions such as the Sabatier process [12] and methanol synthesis [13], and is hence referred to as the “building block stage” [14]. Synthesis gas (CO + H₂), a crucial precursor in the field of C1 chemistry, can be produced using the RWGS reaction in the presence of an appropriate catalyst. The syngas can further be used as a feedstock for the Fischer–Tropsch synthesis reaction (FTS) to produce organic compounds, such as methanol (a crucial component of synthetic fuels and polymers), hydrocarbons, or oxygenated hydrocarbons [15,16]. ExxonMobil recently revealed that its “methanol-to-jet” technology can provide SAF from methanol derived through waste, biomass, captured carbon dioxide, and low-carbon hydrogen [17]. However, further side reactions, such as CO methanation (Equation (2)) [18], could emerge under the same reaction conditions, consuming a large amount of hydrogen. The CO₂ methanation reaction is an exothermic catalytic process that normally takes place at temperatures from 150 °C to 550 °C in the presence of a catalyst [19]. The CO₂ conversion and CH₄ selectivity can almost approach 100%; however, as the temperature rises, the reaction rate increases [20], with preference for RWGS at higher temperature. Therefore, at low reaction temperatures, the highly exothermic methanation reaction is thermodynamically more preferred to the slightly endothermic RWGS reaction [21,22]; hence, reducing methanation throughout RWGS has been a challenging issue. A remaining concern seems to be either the RWGS reaction should be operated at high temperature (over 900 °C), which is thermodynamically favorable, but carbon and undesirable byproducts may also be present; or it should be performed at low temperatures (below 500 °C), in which case it is not kinetically favored but may be made up for by extensive catalyst use [23]. Over the temperature range of 100 to 1000 °C, Kaiser et al. investigated the equilibrium composition of the gaseous products in RWGS reaction for a three-to-one molar H₂/CO₂ input ratio [24]. Based on the results, methanation was thermodynamically preferred at low temperatures (below 600 °C), while, the only product that could form at temperatures beyond 700 °C was CO and very little to no methane. However, to cut down on the energy losses and investment expenses, the temperature must be kept as low as feasible [24]. They proposed that using RWGS at greater pressures in conjunction with high temperature and high-pressure steam electrolysis might be an alternative [24]. Additionally, the FTS normally operates at 2.5 MPa, and the produced syngas or the RWGS supply gas must be compressed [25]. Kaiser et al. came to the conclusion that at this pressure (2.5 MPa), the methane curve was pushed to higher temperatures; for instance, at 900 °C, the equilibrium methane level was 4 mol% as opposed to 660 °C at 1 atm pressure [24]. When Unde et al. tested the Al₂O₃ catalyst through RWGS reaction, they discovered that the CO₂ to CO conversion equilibrium was reached at a high temperature of 900 °C. Reaction was controlled kinetically between 300 and 700 °C, and thermodynamically above this temperature range [26]. As a result, production of active RWGS catalysts operated at low-temperature with higher CO selectivity and limited CH₄ production was required. Insight into the mechanisms of CO production is also vital for rational catalyst design in such processes. Various reaction routes could lead to various kinetic parameters and selectivity variations for CO₂ hydrogenation [27].



According to the concept of microscopic reversibility and the fact that the RWGS reaction is typically carried out at equilibrium, the active catalysts in the water gas shift (WGS) process are also effective in the RWGS reaction, but may be under different reaction

conditions, suggesting that similar catalysts should enhance both reactions [28]. Some typical features of WGS catalysts include the presence of oxygen vacancies, the strength at which CO can be adsorbed, and activity for dissociation of water [29]. In our earlier study, a thorough overview of the most recent advancements of catalysts utilized in low-temperature WGS reactions is presented [30]. In various CO₂ conversion processes, many types of catalysts have been used, including oxide-supported metal catalysts and oxide catalysts in which cerium oxide (CeO₂) has had a key role [30,31]. CeO₂ is a typical rare earth metal oxide with a face-centered cubic (FCC) fluorite structural pattern, and has oxygen storage capacity (OSC) and a number of intriguing features that can be exploited to improve catalytic efficiency [28,32]. In comparison to other reducible oxides, oxygen vacancies on the surface of CeO₂ are more easily formed during the reduction process owing to its unique electron arrangement [33]. Besides, the reversible redox pair Ce³⁺/Ce⁴⁺ and the acid basic surface properties of CeO₂ are effectively leading to its broader catalytic application [34]. It was found that the reducibility of ceria had an inverse connection with the bimetallic cluster promoted local electronic band, which caused the stability of germinal OH groups and was assumed to be the reason for higher WGS activity [35]. Besides, the RWGS reaction has been reported to work well with noble metal-loaded CeO₂ catalysts [36]. In a comparative study, Castao et al. looked at the efficiency of platinum and gold catalysts on ceria supports [37]. Transition metals supported on CeO₂ also have greater RWGS activity than metals supported on non-reducible supports. Moreira et al. investigated the sorption-accelerated WGS process at low temperature (125–295 °C) over Cu-CeO₂/HTlc catalysts; Cu supported on polyhedral nanoparticle-sized ceria displayed a high conversion of 87.6% [38]. Comparing the performances of 1.7% Pt-CeO₂ and Pt-Al₂O₃ at 573 K in WGS reaction, Porosof and Chen examined the amount of CO uptake as an indicator of the dispersion of Pt metal. They found out that the amount of CO uptake using Pt-CeO₂ is ~5.7 times higher than that on Pt-Al₂O₃ [39].

As it is shown in Figure 1, the CeO₂ nanocrystal surface consists of three low-index lattice planes: (100), (110), and (111) [40,41]. The three planes have distinct activity and follow the sequence (100) > (110) > (111), while showing an opposite trend for stability [42–45]. The basis of the face impact of ceria on catalytic function is the variation in electronic properties and surface atomic configuration of ceria, both of which affect the ability of oxygen vacancy formation and the structure of surface intermediates [46–50]. Based on catalytic activity evaluation, CeO₂ alone as a catalyst does not perform well and can only generate a limited number of oxygen vacancies; therefore, adding metal components to CeO₂ improves its reducibility and capacity to create oxygen vacancies [51,52]. The role of ceria in distributing the active phase appears to be particularly important in defining CO selectivity. According to recent findings, large metal particles are generally selective for methane, but well-dispersed smaller nanoparticles are more in favor of the RWGS reaction than methanation [53–55]. The potential of ceria surface to initiate a variety of CO₂ reaction pathways leading to various products is also important in this regard [56,57]. Different synthesis methods [58] and treatment procedures can be used to design and control the shape and size of ceria nanocrystals in order to increase redox characteristics and catalytic activity [59,60].

The use of different catalysts in the RWGS reaction has been considered in some review articles related to the catalytic conversion of CO₂ to chemicals and fuels [61,62]. Porosof et al., for example, looked at several catalysts for converting CO₂ to CO, methanol, and liquid hydrocarbons [63]. Kattel et al. investigated the conversion of CO₂ to the CO products containing C1 only, such as CO, methanol, and methane, with an emphasis on the effect of metal/oxide catalyst interfaces in these processes [64]. Moreover, attempts have been made to review the RWGS reaction mechanism on supported metal and oxide catalysts. For example, Su et al. looked into the RWGS reaction pathways over different types of catalysts (supported metal catalysts (including ceria), mixed oxide catalysts, and transition metal carbide catalysts) [65]. After going through many papers utilizing various catalysts for each type, they found that large volumes of water are generated in all CO₂

hydrogenation processes, and the creation of hydroxyls can poison the catalyst. Therefore, due to the fact that RWGS reaction is typically carried out at a moderate to high temperature, catalysts with great water tolerance are desirable for practical applications [65]. As they suggested, this shortcoming might be resolved by converting CO_2 to CO using the RWGS method and then treating the CO_2 with a moisture separator unit before it enters the subsequent reactor systems [65]. In any case, stable, modern water-tolerant catalysts with affordable facilities are still appealing for direct CO_2 conversion. On the other side, there are several studies describing the principles of CeO_2 , and a number of recent reviews detail their catalytic uses in different CO_2 hydrogenation reactions [66–69].

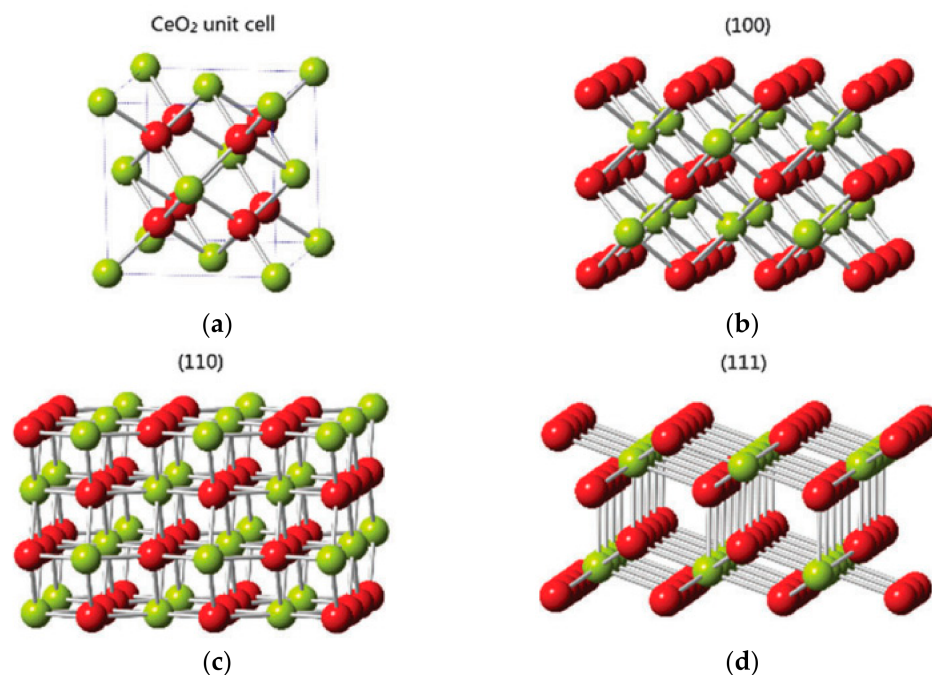


Figure 1. (a) CeO_2 FCC Unit cell, (b–d) the (100) [or (200)], (110), and (111) planes of the CeO_2 structure, reprinted with permission from [41]. Copyright Royal Society of Chemistry, 2014.

Unlike prior studies that provided an overview of several types of catalysts for the RWGS reaction, this review focuses on the function of ceria-supported catalysts in the RWGS reaction for CO_2 valorization, to highlight the benefits and drawbacks of using selected catalytic systems. Besides, the physicochemical properties of supported catalysts, which affect the catalytic activity/stability and CO selectivity in the RWGS reaction, such as the morphologies, metal loading, and metal size, are discussed to explain the structure–activity correlations. The unique significance of ceria in RWGS reaction mechanisms is also discussed with the prospect of developing cost-effective formulations based on ceria oxides to help relevant CO_2 conversion technologies gain market acceptance. In order to comprehend how CeO_2 performs in the RWGS reaction system, a detailed review of reaction mechanism is performed in addition to considering the thermodynamic factors. With all these aspects, the objective of this review is to provide a comprehensive framework for understanding the development of heterogeneous catalysts based on CeO_2 support that successfully catalyze the RWGS reaction. The review also examines the associated challenges and presents the future prospects of this field.

2. Mechanism

According to the literature, the nature of the support has a substantial influence on the reaction mechanism [70,71]. Two RWGS mechanisms have been suggested based on reaction kinetics, spectroscopy, and density functional theory (DFT) simulations; Surface Redox Mechanism and Associative Mechanism [72,73]. Nevertheless, redox and associative mechanisms have been highly controversial since the mechanism is so susceptible to the

catalyst types and reaction conditions. Hence, no clear consensus on the RWGS reaction mechanism has been established yet [74]. The primary step that is different between the two pathways is whether the dissociated H atoms are implicated in the production of carbon-containing intermediates, e.g., formates and carboxyls [75]; the potential chemical pathways are depicted schematically in Figure 2 [76].

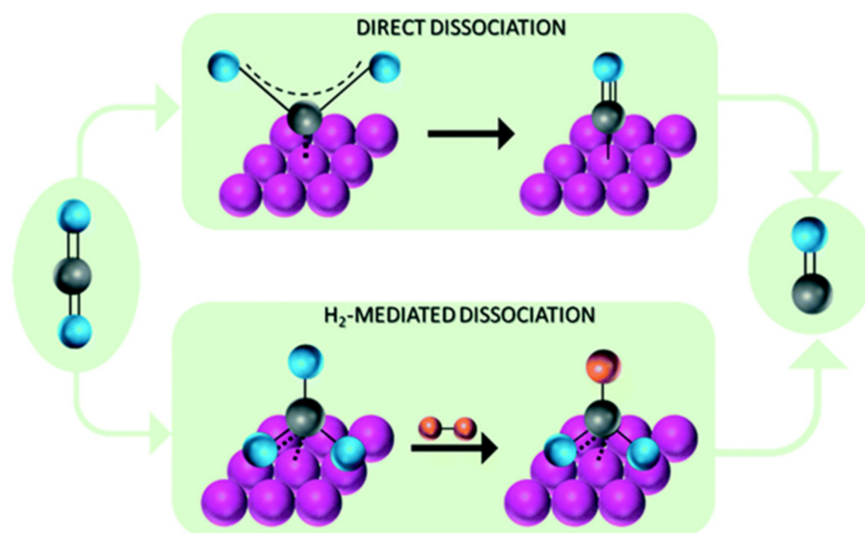


Figure 2. Simple schematic of RWGS mechanism for direct and H-assisted CO_2 dissociation processes, reprinted with permission from [76]. Copyright Royal Society of Chemistry, 2021.

In the redox mechanism, CO_2 is reduced to CO while the catalyst is directly oxidized, and subsequently H_2 reduces the catalyst to fulfill the catalytic turnover (Equations (3) and (4)) [77]. This mechanism is only viable when two essential criteria are met: (i) H_2 can reduce the catalyst surface and (ii) the partially reduced catalyst surface can be reoxidized effectively by CO_2 under RWGS experimental parameters [78]. Reducible oxide catalysts, which have the advantage of being easily reduced and oxidized during the reaction settings due to the fact that oxygen is provided by the support itself, have been found to largely follow this mechanism [79]. In the case of CeO_2 , CO adsorbs on a metal surface and gets oxidized by oxygen atoms from the ceria, before being re-oxidized by water [80]. This mechanism is most commonly reported on Cu-based catalysts. For example, Lin et al. investigated Cu- CeO_2 nanocatalysts in the RWGS reaction and discovered that it follows the redox mechanism to effectively improve CO_2 dissociative activation (Figure 3a) [81].

In another study by Lee et al. a series of catalysts with different CeO_2 and TiO_2 support proportions were synthesized via impregnation [82]. They discovered that in the RWGS reaction over Pt/ CeO_2 - TiO_2 catalyst, the redox and dissociation mechanisms coexisted, and more importantly, adding a proper amount of CeO_2 improved the redox properties and catalytic activity (Figure 3b) [82]. According to Kim et al., the sequencing of the injections affects how much CO is produced [79]. Therefore, Lee et al. measured the CO produced by feeding CO_2 after H_2 for the first run of their step reaction tests and the CO produced by feeding H_2 after CO_2 for the second run in order to investigate the impact of the injection sequence [82]. The results showed that CO production increases when H_2 is added first [82]. The catalytic mechanisms of RWGS on ceria nanocrystal were explored by Liu et al., with a function of oxygen vacancies in ceria being particularly highlighted [83]. CO can be produced by two alternative CO_2 dissociation routes, one of which takes place over ceria oxygen vacancy. As it is concluded by them, in case of ceria, the oxygen vacancy could travel through bulk active oxygen. The oxygen-ion conductivity and density of surface oxygen vacancies were boosted by the apt nanostructure of ceria, which included more exposed active planes and bulk mobile oxygens [83]. Furthermore, adsorbed or dissociated hydrogen can interact with the surface active oxygen of ceria to form water and generate a new oxygen vacancy at the initial location (Figure 3c) [83].

They investigated the mechanism using Ni as an active site supported on CeO₂ and found that CO is directly formed by the dissociation adsorption of CO₂ on the nickel surface (Figure 3d) [83]. Absorbed hydrogen, whether dissociated or not, combines with oxygen species provided by CO₂ dissociation to form water, and then with CO to make CH_x species, e.g., CH₄ [83].



where * stands for a surface site, such as a metal surface site.

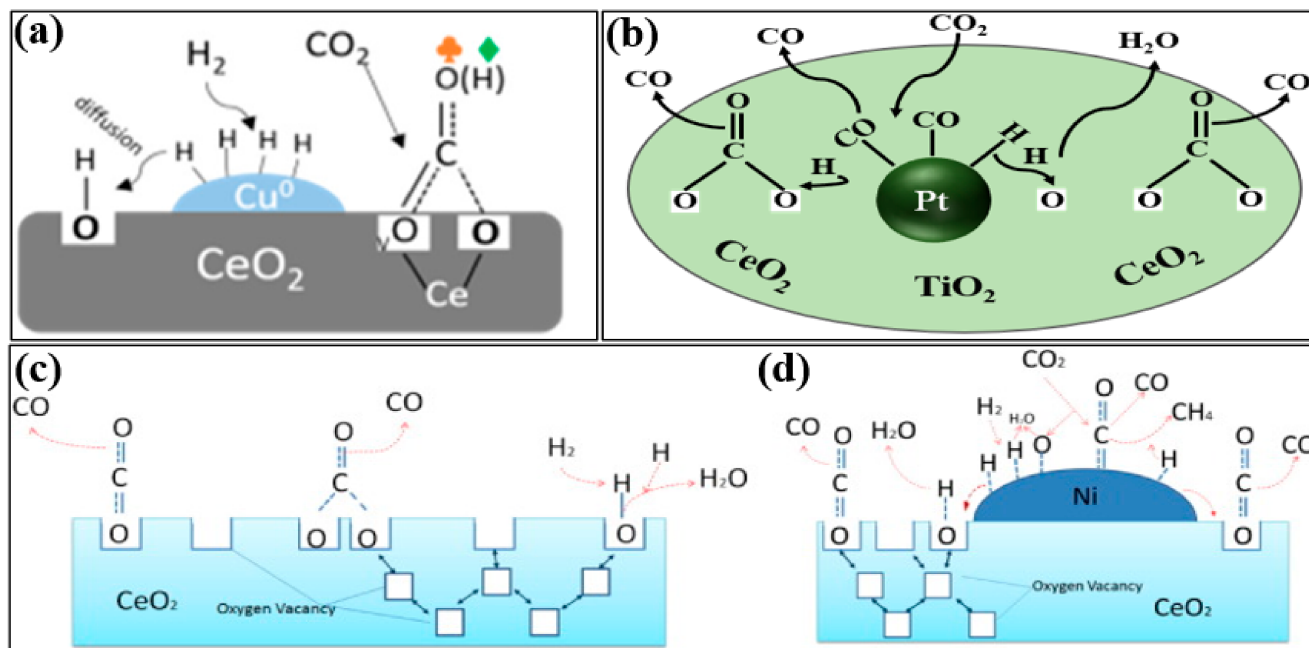


Figure 3. The Redox reaction mechanism of the RWGS reaction over (a) Cu-CeO₂, reprinted with permission from [81]. Copyright ACS, 2018, (b) Pt-CeO₂-TiO₂, (c) ceria nanocube, reprinted with permission from [83]. Elsevier, 2016, and (d) Ni-CeO₂ nanocube, reprinted with permission from [83]. Elsevier, 2016.

The adsorption and dissociation of CO₂ on defects of ceria surface followed by the generation of surface carbonate and formate species are also often postulated as reaction mechanism for the RWGS reaction over ceria-supported catalysts [84]. Cu/CeO₂ catalysts have been found to have significant catalytic activity, probably due to the emergence of intermediates like formates and bidentate carbonates [81]. In this mechanism, known as the “associative mechanism”, CO₂ adsorbs onto the catalyst surface and interacts with dissociated H in order to create transitional molecules such as formate (*HCOO), carboxyl (*COOH), carbonate (CO₃²⁻), and bicarbonate (HCO₃⁻), that will then be degraded to the final RWGS reaction products, CO and H₂O [65]. For example, in a study led by Zhu et al. the reaction over the Au/CeO₂ catalyst was found to follow an associative pathway through a surface formate intermediate, which was proven by DRIFTS and mass spectrometry analysis [85]. In another study conducted by Lu et al., the RWGS reaction mechanism over liquid nitrogen (LN)-CeO₂ catalyst was evaluated resulting in formation of intermediate formates as shown in Figure 4a [86]. They examined the reaction intermediates in the RWGS reaction using in situ FTIR to identify the types of reactants adsorbed and carbonate species generated on LN-CeO₂ catalysts and understand the pathway of the CO₂ hydrogenation process (Figure 5a) [86]. The spectra peaks that they described are presented as follows [86]. The notable peaks between 2200 and 2500 cm⁻¹ could be explained by different types of CO₂ or gas molecules that have been adsorbed on the LN-CeO₂ surface. Two sharp peaks were visible at 3730 and 3628 cm⁻¹, and many small peaks between 3800

and 3000 cm^{-1} can be attributed to the stretching vibration of the OH group on the LN-CeO₂-100 catalysts. The large peaks that appear at frequencies from 2500 and 2800 cm^{-1} centered near 2560 cm^{-1} were caused by the stretching vibration of the COO group of the carboxylate on the LN-CeO₂-100 catalysts. The broad peak, which occurred at 2078 cm^{-1} , was related to CO-Ce³⁺ and was caused by CO adsorption on LN-CeO₂ catalysts. The sharp peak at 1036 cm^{-1} and many smaller peaks around $1020\text{--}1100\text{ cm}^{-1}$ may be linked to the vibration modes of carbonate species produced on the LN-CeO₂ catalyst surface. It is possible to attribute the sharp peak at 1278 cm^{-1} to the bidentate carbonates O-C-O stretching vibration. The peaks, which were the typical peak of formate species, were found approximately at 1600 cm^{-1} , and can be linked to the asymmetric stretching vibration of the O-C-O group. These results indicate that the formate (HCOO[−]) species was formed by LN-CeO₂ catalysts. In this scenario, the intermediate formate (HCOO[−]) species in the CO₂ hydrogenation process could be configured on the LN-CeO₂-100 catalysts, and the formate (HCOO[−]) species passed through deconstruction to release CO at high temperature [87].

The decomposition of formate has long been regarded as a significant pathway for the RWGS reaction. Nonetheless, one of the most essential paths, particularly for reducible oxide-supported metal catalysts, is the carbonate route [88]. Surface carbonates are designated as reaction intermediates, while formates are characterized as “minor intermediates” owing to a stronger bonding and lower exchange rate found in transient isotopic studies [89]. Using in situ DRIFTS experiments, Zhang et al. revealed that CO₂ may be activated efficiently over the Cu-CeO₂ catalyst via the formate and carbonate pathways in the presence of oxygen vacancies [88]. To discover reaction intermediates and speculate the probable reaction routes, Dai et al. performed in situ DRIFTS analysis on a series of Ga₂O₃/CeO₂ composite oxide catalysts with varied Ga₂O₃ and CeO₂ ratios [90]. They concluded that, in case of pure Ga₂O₃ with no CeO₂ the system creates bicarbonate intermediates, which are more likely to hydrogenate to CH₄ at high H₂ levels. The reaction mechanism for composite oxides and CeO₂ may involve the formation of formate, which reacts with H^{*} to generate HCOOH^{*}, dehydrates to produce CO^{*}, and then eventually transforms to CO (Figure 4b) [90]. Li et al. used Cu and Cu-In active metals to get insight into the RWGS reaction mechanisms over the bimetallic catalysts on CeO₂ support [91]. In case of Cu-CeO₂, the rich contact between a highly dispersed Cu, for H₂ dissociation (Equation (5)), and defective CeO₂, for CO₂ activation (Equation (6)), results in a high RWGS activity on CeO₂ (Figure 4c). On the other hand, Cu₅In₅-CeO₂ has lower RWGS activity than Cu₁₀-CeO₂ due to the presence of In, which enhances the level of Cu aggregation and fills oxygen vacancies on CeO₂ (Figure 4d). The catalysts were followed the routes shown in Equations (5)–(8) [91].



Although noble metal-loaded CeO₂ catalysts have been proven to be active for the RWGS reaction, the reaction mechanism remains a point of contention. Earlier research on Pt-CeO₂ catalysts, for instance, has revealed that intermediates like carbonates and formates have an essential part in the reaction, implying an associative mechanism [89,92]. At 300 °C, however, WGS process is predominantly controlled by a redox mechanism over Pt-CeO₂ catalyst [93]. Chen et al. in their research work on Pt-CeO₂ catalyst identified that despite the fact the redox and dissociation mechanisms coexisted in the RWGS reaction over Pt/CeO₂ catalyst, the dissociation mechanism, which involves the creation of intermediates, has been identified as the main pathway for CO generation due to difficulty of the CO₂ molecules adsorbing on Ce³⁺ active sites to directly generating CO (Figure 6a) [94]. In situ reflectance FTIR studies were carried out to gain more understanding of the reaction process and to analyze the generated intermediates during the RWGS reaction (Figure 5b) [94]. The

peaks at 2045 and 1772 cm^{-1} were thought to be responsible for the linear- and bridge-bonded CO on the reduced Pt particles' surface. The peak at 1940 cm^{-1} was attributed to the linearly adsorbed CO at the Pt and CeO_2 contact areas. The spectrum at 2130 cm^{-1} was compatible with the Ce^{3+} –CO assignment, where the CO is adsorbed on Ce^{3+} sites. The peaks of 2830 and 1600 cm^{-1} , respectively, emerged by formation of the formate and carbonate species. Purged by He stream, the evidence of the formates and CO adsorbed on Ce^{3+} sites diminished immediately, whereas the strength of the peaks due to the linearly adsorbed CO at the contact sites and the Pt–CO species faded gradually. This indicates that even while inert gas was flowing, the produced CO was highly adsorbed on certain metals or interfacial sites. In the meantime, there is a weak connection between the produced formate species and the CO adsorbed on Ce^{3+} sites. The findings reveal that it is challenging for the CO_2 molecules adsorbed on Ce^{3+} active sites to produce CO directly (surface redox mechanism). The alternate dissociative pathway is more likely, where the synthesis of formate species as major intermediates is possible via the interaction of adsorbed CO_2 with H_2 that ultimately decomposes into CO [94].

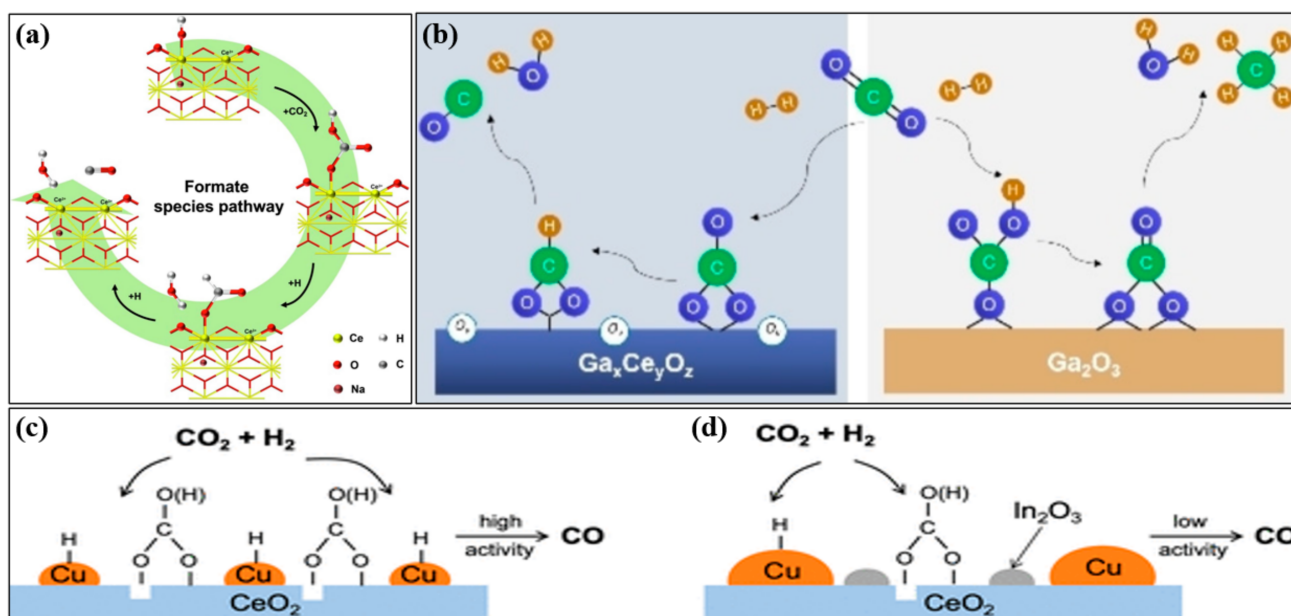


Figure 4. The associative mechanism of the RWGS reaction over (a) LN-CeO₂, reprinted with permission from [86]. Copyright Elsevier, 2022, (b) Ga₂O₃–CeO₂, reprinted with permission from [90]. Copyright Wiley, 2022, (c) Cu–CeO₂, reprinted with permission from [91]. Copyright ACS, 2022, (d) Cu₅In₅–CeO₂, reprinted with permission from [91]. Copyright ACS, 2022.

Goguet et al. investigated the reaction mechanism and intermediates in RWGS using a Pt/CeO₂ catalyst and reported that it followed the redox mechanism [84]. They stated that the RWGS reaction took place through surface carbonate intermediates, with carbonate species forming at the reduced CeO₂ surface (Figure 6b) [84]. On Au–CeO₂ catalysts, heterolytic dissociation is feasible at 150 °C, leading to a hydroxide and gold hydride groups [95]. In order to have a better understanding of the mechanism, Wang et al. conducted research on Au–CeO₂ (Figure 6c,d) [80,96]. In their study in 2013, they found that CO₂ reacts with a pre-reduced Au/CeO₂ catalyst to produce active oxygen, indicating a redox mechanism for the RWGS reaction at temperatures over 200 °C (Figure 6c) [80]. Later, in their published work in 2015, they concluded that even though it was thought that the RWGS reaction was dominated by an associative reaction pathway, some evidence of redox mechanism was seen in the RWGS reaction at temperatures above 120 °C (Figure 6d) [96].

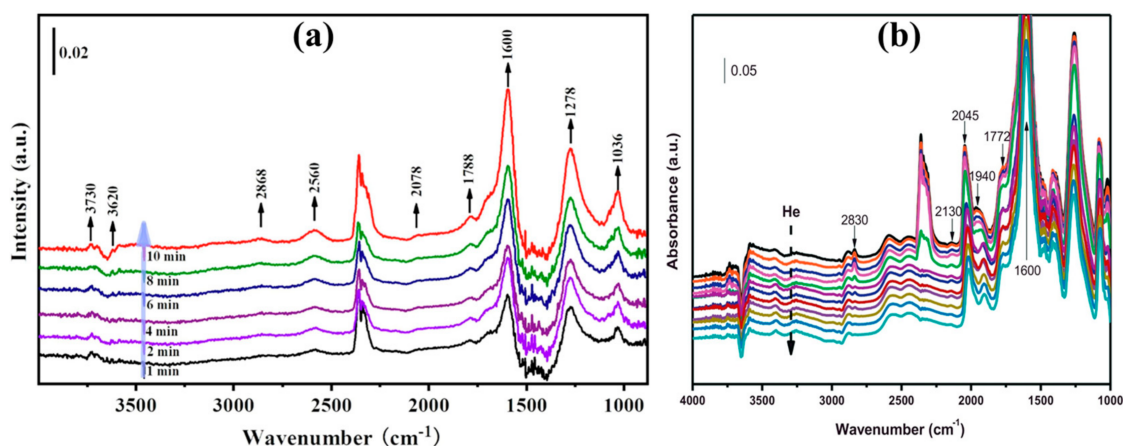


Figure 5. Operating DRIFT spectra captured after injecting a CO_2/H_2 mixture: (a) LN-CeO₂, reprinted with permission from [86]. Copyright Elsevier, 2022, (b) Pt-Ce catalyst calcined at 500 °C, reprinted with permission from [94]. Copyright Elsevier, 2016.

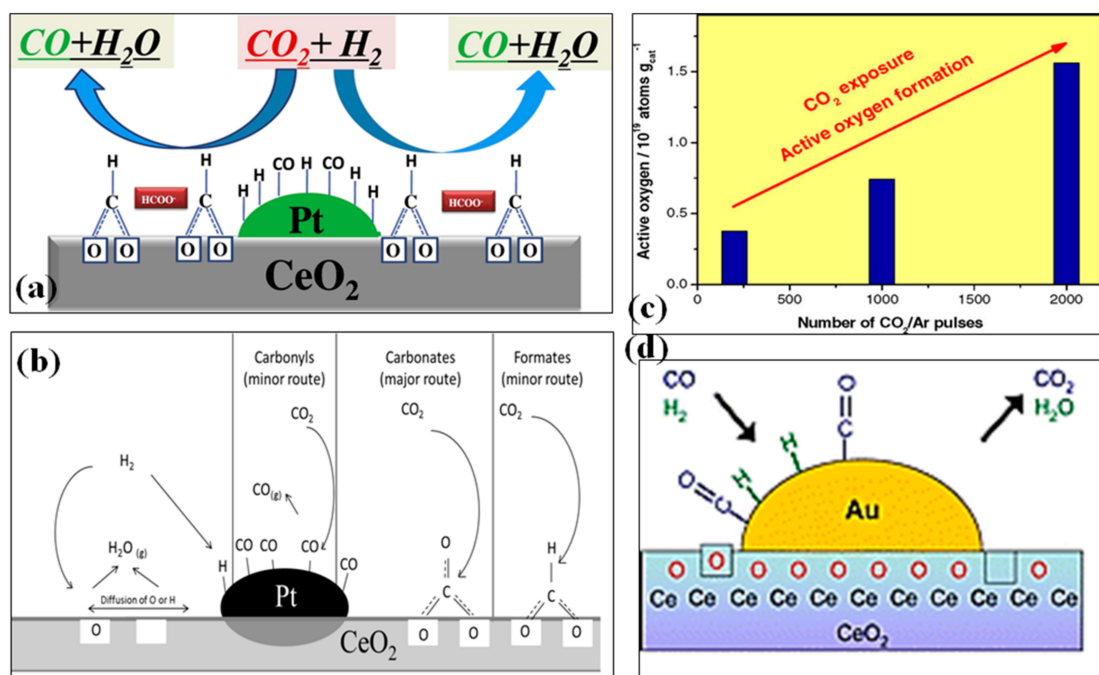


Figure 6. Model for the reaction mechanism of the RWGS reaction over (a) Pt-CeO₂, reprinted with permission from [94]. Copyright Elsevier, 2016, (b) Pt-CeO₂, reprinted with permission from [84]. Copyright Elsevier, 2004, (c) Au-CeO₂, reprinted with permission from [80]. Elsevier, 2013, (d) Au-CeO₂, reprinted with permission from [96]. Copyright Royal Society of Chemistry, 2015.

There are some reports indicating the reaction to follow neither of the two dominant pathways. Shen et al., for example, investigated the mechanism on the Ni-CeO₂ catalyst in the RWGS reaction and proposed a novel perspective into the reaction mechanism (Figure 7), arguing that CO₂ was initially adsorbed on the hydroxyl groups of Ce³⁺-OH rather than oxygen vacancies (1, 2), resulting in the formation of the bicarbonate intermediate (*HCO₃) (3). The bicarbonate intermediate was then converted to formate (*HCOO) (4), with CO being generated by the highly active H⁻ in Ce-H (5) [97]. According to DFT and DRIFTS investigations, the high selectivity is attributed to the low CO affinity, but the higher catalytic activity is due to the abundance of C-H species [97].

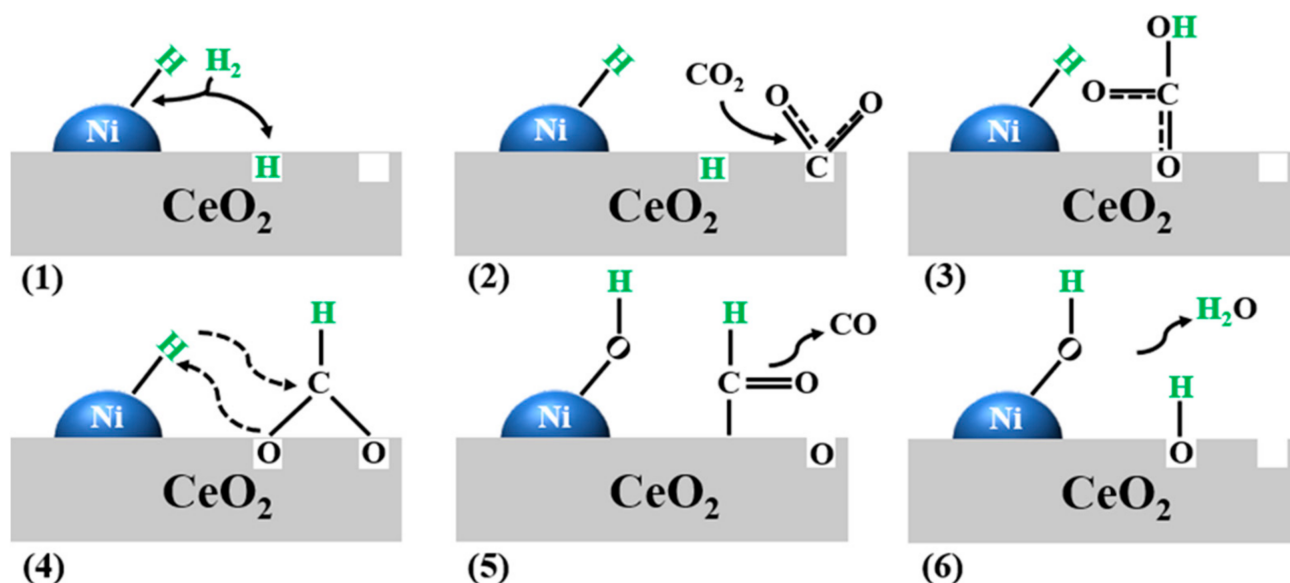


Figure 7. The proposed reaction mechanism of the RWGS reaction over Ni-CeO₂ catalyst.

Deng et al. synthesized 10Ga5Cu-CeO₂ catalyst using direct pyrolysis for photo-thermal catalytic RWGS reaction and identified the mechanism by in situ DRIFTS (Figure 8a) [98]. It revealed that the addition of Ga increased the synthesis of formate species, which are essential intermediates in CO₂ hydrogenation, and light irradiation promoted the breakdown of formate species to carbonyl, resulting in increased CO generation [98]. In contrast, by using Ga₂O₃ as a catalyst for the RWGS reaction after adding an amount of CeO₂ as a promoter, Zhao et al. established that adding CeO₂ to the reaction increased the development of bicarbonate species intermediates that could form H₂O and CO by interacting with H dissociated on the Ga₂O₃ surface [99]. Yang et al. provided a unique approach for boosting RWGS rate under H₂ lean conditions at low temperatures, in which they evaluated a % Cu-CeO₂ catalyst under visible light illumination, which increased catalytic activity by 30% at 250 °C (Figure 8b) [100]. Using various techniques and analysis, they discovered that, under visible light irradiation, the localized surface plasmon resonance (LSPR) created by Cu nanoparticles induces heated electron transfer to ceria, triggering desorption of bidentate formate and linear-CO transition specie [100].

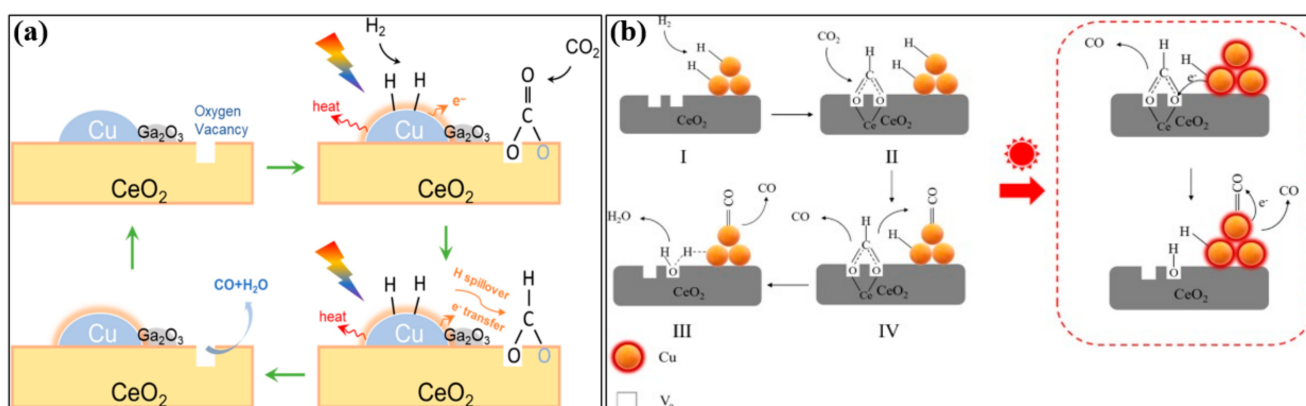


Figure 8. The associative mechanism of the RWGS reaction over (a) 10Ga5Cu-CeO₂, reprinted with permission from [98]. Copyright Elsevier, 2021, (b) Cu-CeO₂, reprinted with permission from [100]. Copyright Elsevier, 2022.

These possible alternatives indicate that there is no universal mechanism in RWGS reaction, and the reaction pathway is highly sensitive to the active metals/oxides, supports, and reaction conditions. Therefore, condensing such data into a table that succinctly explains the impact of the selectivity or functionality of active metal oxide on RWGS reaction mechanism is beneficial (Table 1).

Table 1. Dominated mechanism in RWGS reaction based on different kinds of metal-CeO₂.

Active Metal	Mechanism	Ref.
Cu	Redox or Associative	[81,91,100]
Cu ₅ In ₅	Associative	[91]
Ni	Redox	[83]
Ga	Associative	[90]
Pt	Redox and/or Associative	[84,94]
Au	Redox and/or Associative	[80,96]
10Ga ₅ Cu	Associative	[98]
Ce	Redox	[83]

3. Kinetics of RWGS Reaction

An understanding of reaction kinetics is necessary for designing a practical reactor. The majority of stated kinetic rate formulations for CO₂ hydrogenation reactions are based on Langmuir-type expressions since various reactions occur and adsorption factors influence the kinetics [101]. Interestingly, CO₂ RWGS is reported to be a faster process with a lower activation energy than the WGS reaction on many of the metal/oxides [102,103]. Recently, much research on the activity and stability of different active metals using CeO₂ support has been performed on the RWGS reaction; however, just a few kinetic and mechanistic studies have been reported on the RWGS reaction [104–106]; in most cases, the Langmuir kinetic model or power law equations have been used to explain the reaction kinetics.

Poto et al. adopted single-, dual-, and three-adsorption-site to model the kinetics of CO₂ hydrogenation to methanol over a Cu-CeO₂/ZrO₂ catalyst [107]. The findings reveal that H₂ is adsorbed and dissociated on Cu⁰ sites, whereas CO₂ is drawn to the oxygen vacancies formed by the CeO₂-ZrO₂ solid solution. Following that, the adsorbed H interacts selectively with the carbon atom, preferring the “formate” pathway. The CO produced by the RWGS process could desorb to the gas phase or undergo hydrogenation to yield methanol. Table 2 shows the suggested rate equations for the RWGS, where k_i is the kinetic constant and b_i adsorption constants of i compound. The reaction rate law, first proposed by Henkel [108], was later modified by Graaf et al. [109]. The results showed that the reaction rates rise noticeably with the H₂/CO₂ concentration ratio and exponentially with temperature. They found that higher reaction rates and less H₂ consumption in the feed could be obtained from a more hydrophobic surface due to a lower H₂O adsorption and higher desorption rate from Cu⁰ sites on such surfaces [107]. In order to increase the resilience of the model results, they developed a process that evaluated the sensitivity of models to the preliminary data. This method included repeatedly conducting the optimization algorithm (as a loop), with recently obtained results serving as the initial guesses. Based on the examination, it was determined that the kinetic model satisfied the physicochemical restrictions [107]. To speed up reactions and decrease the demand for H₂ in the feed, the authors suggested a more hydrophobic surface which may exhibit faster desorption from Cu⁰ sites and weaker H₂O adsorption [107]. Unfortunately, very few investigations have looked into the reaction rate of M-CeO₂ catalysts in RWGS reaction; hence, the following studies will compare the reaction rates of several catalytic systems in order to gain insight into the kinetics of the RWGS reaction and the factors that affect the rate of CO₂ conversion into CO.

Lalinde et al., studied the RWGS reaction kinetics using an ordered-mesoporous Ni-Al₂O₃ catalyst [110]. Within the studied temperature range, they found that the rate equation for the RWGS reaction (Table 2) also comprises the WGS reaction, owing to the low equilibrium constant ($K_{eq,RWGS} = 0.03$ and 0.1 at $320\text{ }^{\circ}\text{C}$ and $420\text{ }^{\circ}\text{C}$, respectively,) and formation of CO being the rate-determining step (RDS) [110]. In their proposed reaction rate the parameters are: $k_2 = k_{CO} \cdot k_{CO_2}$ as rate constant, k_{β} as the theoretical gas phase equilibrium compared to the equilibrium on the catalyst surface, and p_i as partial pressure of species i in gas mixture (bar). The experimental results and the local concentrations predicted by models were in good agreement [110]. Moreover, the results were consistent with another similar work by Kopyscinski et al. [111]. The reaction orders and the RDS can change depending on reaction parameters [112]. For example, reaction orders involving P_{H_2} and P_{CO_2} alter as the partial pressures of the gases change [104,105,113]. Ginés et al. investigated the reaction rate on the CuO-ZnO/Al₂O₃ catalyst as well as establishing a relationship between the reaction orders for H₂ and CO₂ in the RWGS reaction [105]. They confirmed that over a $P_{CO_2}:P_{H_2}$ ratio of less than 1:3, the reaction rate was strongly sensitive to P_{CO_2} (order of 1.1) and irrespective to H₂ (0 order), probably owing to surface deconstruction that favors CO₂ dissociation. Whereas, at a moderate ratio of partial pressures (>1:3), they suggested that the reaction rate is reliant on both gases with order of 0.3 for P_{CO_2} and 0.8 for P_{H_2} . The terms in their proposed reaction rate (provided in Table 2) are as follows: X denotes CO₂ conversion and L_0 indicates the amounts of active sites in a fresh sample [105]. Kim et al. found that the RWGS reaction kinetics with Pt-reducible supports, e.g., Pt-TiO₂ and Pt-Al₂O₃ synthesized by impregnation method, were compatible with the redox mechanism [79,114]. The suggested reaction rate, as presented in Table 2, was developed using C_t as the concentration of active sites in unused catalysts [79]. Using a commercial Pt-Al₂O₃ catalyst this time, Jadhav et al. studied the RWGS reaction kinetics and impact of reaction parameters on catalyst efficiency, and discovered that increasing pressure increased CO₂ conversion value [115]. The reactor was tested in varied reaction settings to see how the temperature and H₂/CO₂ ratio in the feed affected reaction rate. It was realized that as the H₂ concentration in the feed increased (the partial pressure of hydrogen increased) a higher CO₂ conversion and reaction rate were achieved. Moreover, at the same P_{H_2}/P_{CO_2} , as the temperature increased from 573 to 673 K, the reaction rate rose from 0.009 to 0.044 mol/h/g [115]. In addition, the conversion values calculated in this study were lower than those obtained by Kim et al. using impregnated Pt-Al₂O₃ [79,115]. Ghodoosi et al. used a redox kinetic model over the Fe-Mo/Al₂O₃ catalyst for the RWGS reaction in a fixed-bed reactor to develop their rate model to describe the reaction kinetics [116]. They looked at the influence of feed gas temperature and discovered that, at high feed temperatures, the temperature drop in the reactor rises. The reason is, with increasing gas mixture temperature in feed, the rate of the reaction increases and because of the endothermic nature of RWGS reaction, it consumes more heat, causing the temperature to decrease [116]. In order to assess the proposed reactor model, three sets of experimental data were used. The outcomes demonstrated a good consistency between the model predictions and experimental findings under non-equilibrium conditions, with an average deviation of 2.7%, and an average absolute inaccuracy of 5.6%, proving that the suggested model can effectively predict the operation of the fixed-bed reactor for the catalytic RWGS reaction [116]. In another study, Chen et al. employed atomic layer epitaxy (ALE) as an alternate approach to synthesize homogenous Cu nanoparticles supported on SiO₂ [117]. The RWGS pathway using ALE-Cu/SiO₂ catalysts proceeded via a formate transition species, and the CO₂ and CO adsorption sites for the forward and reverse mechanisms were independent [117]. Najari et al. synthesized Fe-K/ γ -Al₂O₃ catalysts via the impregnation method to perform the RWGS reaction in a lab-scale fixed-bed reactor [118]. Based on their observations, they suggested the use of the Artificial Bee Colony (ABC) method to predict kinetic values and utilize Differential Evolution (DE) optimization methods based on the Langmuir–Hinshelwood–Hougen–Watson (LHHW) mechanism to meet the kinetic requirements [118]. The ABC method outperformed the DE algorithm in forecasting total

hydrocarbon selectivity, with an error rate of 6.3% compared to 32.9%. As a result, the ABC model was used to analyze the distribution of the products. Results showed that at 573 K and 1 MPa, a maximum selectivity of 73.21% for hydrocarbons can be reached with a 0.85% inaccuracy compared to the experimental result of 72.59% [118]. The proposed reaction rate (presented in Table 2), is similar to their other works [61,119]. As per their evaluations, the kinetic parameters obtained by using the ABC algorithm were roughly in line with those published in earlier investigations, taking into account the different catalytic characteristics and reaction conditions [118]. More research is required to fully comprehend how critical factors affect reaction rate and distribution of products. Using the same catalyst, but the two-step incipient wetness impregnation technique, Brübach et al. developed a new LHHW type kinetic rate statement for RWGS reaction [120]. The best performing model was derived under the assumption of H-assisted CO₂ and H-assisted CO dissociation mechanisms, supported by recent mechanistic studies. The statistical analysis demonstrated a significant association between the inhibition coefficients and reaction rate constants, as well as some lack of certainty in the estimated parameters. Since LHHW expressions have a mathematical structure, it is unfortunate that this seems to be inevitable. At a similar actual flow rate, pressure changes from 10 to 20 bar resulted in a considerable increase in CO₂ conversion. Nevertheless, they believed this was primarily due to an increase in residency time. Increasing the temperatures accelerated the reaction rate and pushed the CO selectivity to higher values for the same CO₂ conversion rate. A similar impact was seen when the H₂/CO₂ ratio was increased [120].

Table 2. Proposed reaction rate for some catalysts in RWGS reaction.

Catalyst	RWGS Reaction Rate	Assumption	Ref.
Cu-CeO ₂ /ZrO ₂	$r_2 = \frac{k_2 b_{CO_2} P_{CO_2} P_{H_2} (1 - \frac{P_{CO} P_{H_2} O}{P_{CO_2} P_{H_2} k_2^{eq}})}{(1 + b_{CO} P_{CO} + b_{CO_2} P_{CO_2}) (P_{H_2}^{0.5} + b_{H_2O/H_2} P_{H_2O})}$	- Dual-site LHHW mechanism	[107]
Ni-Al ₂ O ₃	$r_{RWGS} = \frac{k_2 \cdot P_{CO_2} \cdot k_{H_2}^{0.5} \cdot P_{H_2}^{0.5} \cdot (1 - (k_{\beta} \cdot \frac{P_{CO} \cdot P_{H_2} O}{P_{CO_2} \cdot P_{CO_2} \cdot k_{eq, RWGS}}))}{(1 + k_C \cdot P_{CO_2}^e \cdot k_{H_2}^f \cdot P_{H_2}^G + \sqrt{k_{H_2} \cdot P_{H_2} + k_{OH} \cdot \frac{P_{H_2} O}{\sqrt{P_{H_2}}}})^2}$	- CO ₂ dissociation as RDS - The rate equation also includes WGS reaction - Langmuir–Hinshelwood mechanism	[110]
CuO-ZnO/Al ₂ O ₃	$r = \frac{k_1 L_0 P_{CO_2}^0 (P_{H_2}^0 (1-X)^2 - \frac{P_{CO_2}^0 X^2}{k})}{P_{H_2}^0 (1-X) + \sqrt{k_2 P_{H_2}^0 1.5 (1-X)^{1.5} + \frac{P_{CO_2}^0 X}{k_2 k_3}}}$	- CO ₂ dissociation as RDS - Langmuir–Hinshelwood mechanism	[105]
Pt-TiO ₂ Pt-Al ₂ O ₃	$r = \frac{k_A k_b C_t (P_{CO_2} P_{H_2} - P_{CO} P_{H_2} O / k_{eq})}{(k_A P_{CO_2} + k_{-A} P_{CO} + k_{-b} P_{H_2} O)}$	- CO ₂ dissociation as RDS - Adsorption of CO and H ₂ O at the site of catalytic activity was not counted - At low P _{H2} (1 < P _{H2} ⁰ /P _{CO2} ⁰ < 4) the dissociation adsorption phase was not included - Langmuir–Hinshelwood and surface redox mechanisms	[79]
Pt-Al ₂ O ₃	$r = \frac{C_S (k_1 k_2 P_{CO_2} P_{H_2} - k_{-1} k_{-2} P_{CO} P_{H_2} O)}{k_2 P_{H_2} + k_{-1} P_{CO}}$	- In low CO ₂ conversions - Surface redox mechanism and associative formate mechanism - Steady state; r = r ₁ = r ₂	[115]
FeMo-Al ₂ O ₃	$-r_{CO_2} = \frac{k (P_{CO_2} - \frac{P_{CO} P_{H_2} O}{k_{eq} P_{H_2}})}{1 + k_{H_2O} \frac{P_{H_2} O}{P_{H_2}}}$	- Redox kinetic model	[116]
AlE-Cu/SiO ₂	$r = 2^{1/2} k_4 k_1^{1/2} k_2^{1/2} k_3 P_{H_2}^{1/2} P_{CO_2}^{1/2}$	- HCOO-2S → CO-S + OH-S is RDS - Langmuir–Hinshelwood model	[117]

Table 2. Cont.

Catalyst	RWGS Reaction Rate	Assumption	Ref.
Fe-K/ γ -Al ₂ O ₃	$r_{\text{RWGS}} = k_{\text{RWGS}} \frac{P_{\text{CO}_2} P_{\text{H}_2} - P_{\text{CO}} P_{\text{H}_2\text{O}} / k_{\text{eq}}}{P_{\text{CO}} + A_{\text{RWGS,H}_2\text{O}} P_{\text{H}_2\text{O}} + B_{\text{RWGS,CO}_2} P_{\text{CO}_2}}$	<ul style="list-style-type: none"> - LHHW mechanism - One-dimensional heterogeneous model - Steady-state conditions - CO₂ dissociation as RDS 	[118]
Fe/K@ γ -Al ₂ O ₃	$r_{\text{RWGS}} = \frac{k_{\text{RWGS}} (P_{\text{CO}_2} P_{\text{H}_2}^{0.5} - \frac{P_{\text{CO}} P_{\text{H}_2\text{O}}}{k_{\text{eq}} P_{\text{H}_2}^{0.5}})}{(1 + A_{\text{RWGS}} \frac{P_{\text{H}_2\text{O}}}{P_{\text{H}_2}})^2}$	<ul style="list-style-type: none"> - Elementary reaction steps - LHHW mechanism - H-assisted CO₂ and CO dissociation mechanisms 	[120]

4. Effect of Different Parameters on Catalyst Performance in RWGS Reaction

4.1. Preparation Methods

The method of catalyst preparation determines the metal-support interaction and morphological properties of the final catalysts that considerably impact the performance of the catalysts. The impact of different preparation procedures of 1 wt.% Ni-CeO₂, e.g., co-precipitation (CP), deposition-precipitation (DP), and impregnation (IM) approaches, on the physicochemical and catalytic characteristics in the RWGS reaction was explored by Luhui et al. [121]. The Ni-CeO₂-CP catalyst achieved the highest conversion rate in the RWGS reaction when compared to the Ni-CeO₂-DP and Ni-CeO₂-IM catalysts (Figure 9a); however, the CO selectivity followed the order: Ni-CeO₂-IM > Ni-CeO₂-CP > Ni-CeO₂-DP (Figure 9b). As confirmed by TPR analysis, an integration of numerous oxygen vacancies and broadly dispersed small NiO particles was considered to be the reason for the outstanding performance of the Ni-CeO₂-CP catalyst in terms of high activity and good selectivity. This suggests that more nickel ions were integrated into the CeO₂ lattice to develop a solid solution. The Ni-CeO₂-DP catalyst has only a limited number of oxygen vacancies in comparison to the Ni-CeO₂-CP catalyst, which results in low RWGS selectivity. It was proposed that the RWGS selectivity was strongly influenced by the oxygen vacancies. It is believed that the solid solution of Ce_xNi_yO is produced when the Ni²⁺ ions are inserted into the ceria lattice to substitute certain Ce⁴⁺ cations [121]. Oxygen vacancies are produced by the lattice distortion and charge imbalance that occur within the CeO₂ structure [122,123]. Several reports have indicated that precipitated ceria-based catalysts have distinct properties depending on the precipitants used, which significantly influence structural properties and catalytic performance [124–129]. In other work by the same group, Luhui et al. used the CP method to make a range of Ni-CeO₂ catalysts using Na₂CO₃, NaOH, as well as a combination of precipitants (Na₂CO₃:NaOH; 1:1 ratio) in order to investigate their catalytic efficacy in the RWGS reaction [130]. According to the structural characterization findings, the catalyst developed by the mixed precipitating agents (Na₂CO₃:NaOH; 1:1 ratio) exhibited the highest oxygen vacancies along with high Ni particle dispersion, resulting in the highest catalytic activity for the corresponding catalyst (Figure 9c), whereas the precipitants' catalytic selectivity for CO were ranked as: NaOH > Na₂CO₃ > Na₂CO₃:NaOH = 1:1 (Figure 9d) [130]. The technique used to synthesize the CeO₂ catalyst has a substantial impact on its structure, and the structure of the synthesized catalysts can greatly influence the catalytic performance in the CO₂ RWGS reaction [131]. Hard-template (HT), complex (CA), and precipitation strategies (PC) were used to synthesize CeO₂ catalysts with various structures, and their efficiency in the CO₂ RWGS reaction was examined by Dai et al. [131]. The Ce-HT catalyst had the greatest CO₂ RWGS reaction activity due to its porous structure (TEM), high specific surface area of 144.9 m².g^{−1} (BET), and abundance of oxygen vacancies; Ce-HT > Ce-CA > Ce-PC is the temperature sequence in which the catalysts reduce in the presence of H₂ at low temperatures (H₂-TPR) [131]. Xiaodong et al. carried out the RWGS reaction over Pt-CeO₂ catalysts at temperatures between 200 and 500 °C under atmospheric pressure and various pretreatment conditions using the co-precipitated technique [94]. The

samples were represented as PC-M-N, where PC stands for the co-precipitated 1%Pt-CeO₂ catalyst and M and N stand for the calcination and reduction temperatures of the samples, respectively, (Figure 9e) [94]. The catalyst prepared at a lower calcination temperature (PC-500-400) demonstrated a more favorable catalytic performance than the others due to its high Pt dispersion [94]. In another study, Ronda-Lloret et al. investigated the use of metal organic frameworks (MOFs) as precursors instead of merely using the traditional wet impregnation (WI) method in the production of CuO_x-CeO₂ catalysts [132]. After impregnating Cu-MOF using a ceria precursor, they flash-pyrolized (PF) the impregnated MOF applying distinctive conditions and procedures and compared the performances in the RWGS reaction with the WI synthesis technique finding that the MOF-derived catalyst outperformed the other catalyst (Figure 9f) [132]. Throughout the thermal decomposition procedure, the metal ions in MOFs are transformed into metallic or metal oxide nanoparticles, while the organic linkers produce carbonaceous formations which can function as supports and promote active phase distribution [133]. As Ronda-Lloret et al. concluded, by changing the pyrolysis environment, an oxidizing environment may be produced that prevents sintering and keeps copper oxidized during decomposition. Using air in the decomposition process causes the creation of copper oxide compounds that sinter with more difficulty than the metallic copper. This promotes the interaction with the ceria support, which improves its catalytic behavior. Thus, by utilizing air, highly dispersed CuO on CeO₂ can be created that is readily reducible and exhibits strong interactions with the ceria [132].

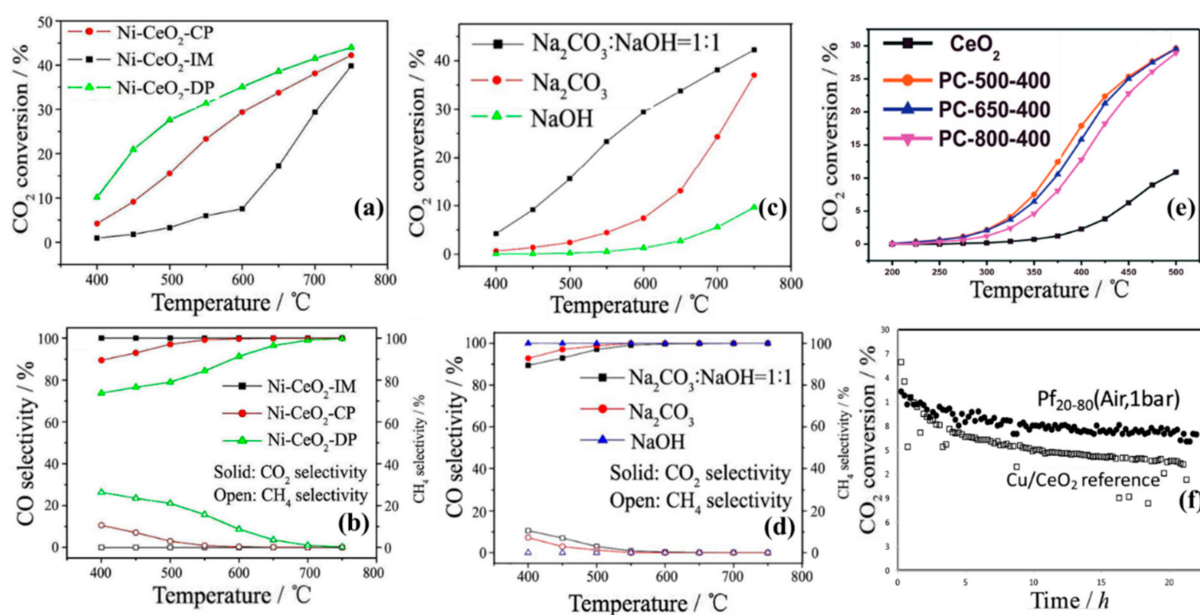


Figure 9. Effect of preparation methods on metal-CeO₂ RWGS reaction: (a) Ni-CeO₂ -activity, reprinted with permission from [121]. Copyright Elsevier, 2013, (b) Ni-CeO₂-selectivity, reprinted with permission from [121]. Copyright Elsevier, 2013, (c) Ni-CeO₂ -activity, reprinted with permission from [130]. Copyright Elsevier, 2013, (d) Ni-CeO₂-selectivity, reprinted with permission from [130]. Copyright Elsevier, 2013, (e) Pt-CeO₂, reprinted with permission from [94]. Copyright Elsevier, 2016, (f) CuO_x-CeO₂-activity, reprinted with permission from [132]. Copyright Elsevier, 2018.

4.2. Shape and Crystal Face Effect

The form and exposed crystal face of catalysts have a major impact on RWGS reaction activity since they may control the adsorption and desorption energies of precursors in the reaction process [134–136]. Thus, the efficiency of CeO₂ supported catalysts can be modified by conducting experiments with various morphologies. The RWGS reaction was studied by Kovacevic et al. over cerium oxide catalysts of various morphologies: cubes, rods, and particles [137]. Using TPR they found that surface oxygen is less removable in the case of nanoshapes with a high concentration of oxygen vacancies and, compared

to rods and particles, cerium oxide cubes had twice more activity per surface area. The stronger intrinsic reactivity of (100) crystal planes encapsulating cubes, as opposed to less intrinsically reactive (111) facets exhibited in rods and particles, results in enhanced catalytic activity of ceria cubes in RWGS [137]. In another study, Lin et al. found that under similar conditions and the same active metal, the $\text{CeO}_2(110)$ surface has substantially more activity than the $\text{CeO}_2(111)$ surface, indicating that the ceria support performance is facet-dependent (Figure 10a,b) [81]. According to their study, once Cu particles are loaded onto the CeO_2 -Nanorod (NR) and CeO_2 -Nanosphere (NS) surfaces, the NR sample exhibits greater RWGS reaction activity. This is mostly due to the increased feasibility of CO_2 dissociative activation and the generation of active bidentate carbonate and formate intermediates over $\text{CeO}_2(110)$ [81]. Liu et al. used RWGS to compare crystal plane reactive activity in three nano- CeO_2 s with varied exposed planes [83]. The overall order of RWGS reactive efficiency of the three studied CeO_2 shapes was ceria nanocube (NC) > ceria-NR > ceria-nanooctahedra (NO), as shown in Figure 10c [83]. It is well established that oxygen vacancies formation on ceria (100) or (110) consume less energy than creating them on ceria (111) [138,139]. As a result, the ceria (100) and (110) planes seem to be more attractive choices for catalyzing processes that involve an oxygen cycle with adsorbates [83]. This could be the main reason why the ceria-NC exposed (100) plane had the best CO_2 conversion and selectivity.

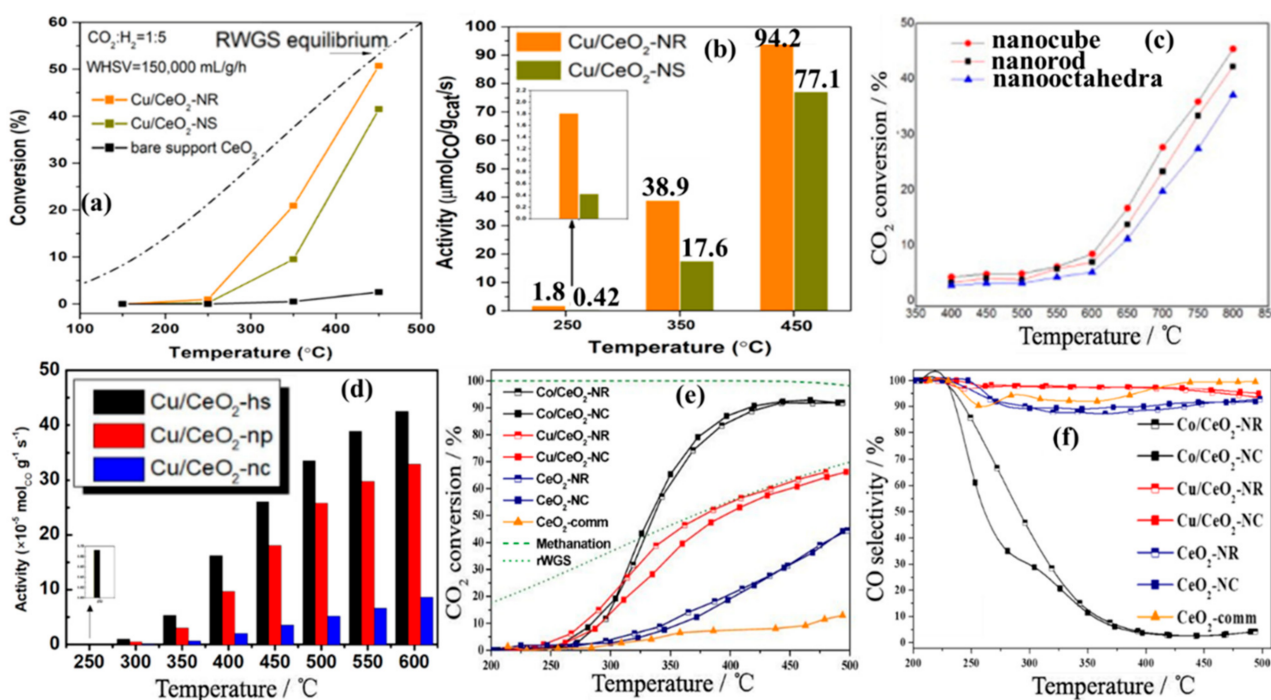


Figure 10. Effect of shape and crystal face on metal- CeO_2 RWGS reaction: (a,b) Cu- CeO_2 , reprinted with permission from [81]. Copyright ACS, 2018, (c) CeO_2 , reprinted with permission from [83]. Copyright Elsevier, 2016, (d) Cu- CeO_2 , reprinted with permission from [88]. Copyright Elsevier, 2020, (e,f) M- CeO_2 (M = Co or Cu), reprinted with permission from [140]. Copyright MDPI, 2019.

Zhang et al. developed self-assembled CeO_2 with 3D hollow nanosphere (hs) (111), nanoparticle (np) (111), and nanocube (nc) (200) morphologies that were employed to support Cu particles [88]. Owing to the large levels of active oxygen vacancy sites, the Cu- CeO_2 -hs(111) exhibited the greatest RWGS catalytic activity among the studied catalysts (Figure 10d) [88]. Konsolakis et al. looked into the influence of the active phase type and ceria nanoparticle support morphology (NR or NC) on the physicochemical characteristics and CO_2 hydrogenation capability of M- CeO_2 (M = Co or Cu) composites at 1 atm [140]. Regardless of support structure, CO_2 conversion was reported to follow the following order: Co- CeO_2 > Cu- CeO_2 > CeO_2 with the Cu- CeO_2 sample being far more selective toward CO

than Co-CeO₂ (Figure 10e,f). The Co catalysts supported on NC ceria demonstrated slightly higher catalytic activity than Co supported on rod-like forms, highlighting the importance of support morphology in addition to the choice of metal element; for Cu-based samples and bare CeO₂, the pattern was the opposite [140].

Figure 11 displays the lattice characteristics of cerium oxide under various conditions based on the work of Lin et al. [81]. To assess the reduction level of support, nonthermal lattice expansion of cerium oxide was used (which represents the creation of Ce³⁺ in the bulk phase). Ceria lattice constant would rapidly drop when the reduced catalysts were exposed to reactant gas at room temperature, suggesting that the oxygen vacancies were regenerated by CO₂ breakdown on the surface of the catalyst. As marked with red squares in Figure 11, in reaction settings and in temperatures ranging from 45 to 110 °C, the CeO₂ lattice of Cu/CeO₂-NR shrank significantly with temperature. Cu/CeO₂-NS, however, had a small rise in the lattice parameter. This behavior suggested that, at low temperatures, Cu/CeO₂-NR was more favorable for CO₂ activation than Cu/CeO₂-NS [81].

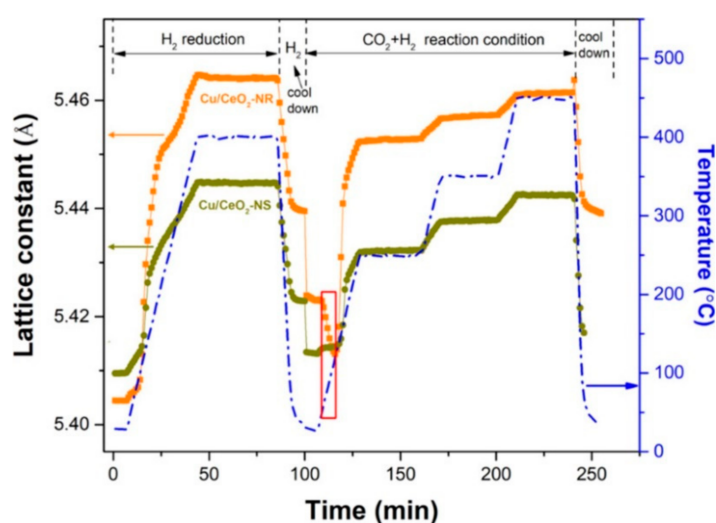


Figure 11. CeO₂ lattice constant for Cu/CeO₂-NR and Cu/CeO₂-NS catalysts, reprinted with permission from [81]. Copyright ACS, 2018.

4.3. Metal–Support Interactions

Activation of catalysts by pretreatment at high-temperature in the presence of hydrogen is often adopted to reduce the oxide nanoparticles and generate oxygen vacancies on the reducible support surface; however, such activation procedures can develop greater interactions between metal nanoparticles and the support, which has been reported to impact catalytic activity in varying ways: positively [141], negatively [142], or in some cases insignificantly [143]. The strong metal–support interaction (SMSI) phenomenon, which typically develops in metals and reducible oxides subjected to high reduction temperature, is one such case [144]. The type of the support [145], metal composition [146], and catalyst synthesis procedure can all influence metal–support interaction (MSI) [147]. According to Goguet et al., the major active site in the RWGS reaction over Pt-CeO₂ catalyst is the interface among Pt and CeO₂ and the reducible site of CeO₂, which is created by the SMSI effect of Pt and CeO₂ [84].

SMSI between Cu species and CeO₂ helps in boosting the reducibility and stability of associated catalysts, which is favorable for catalytic reduction processes [148]. The results of a study by Zhou et al. showed that the H₂ reduction at 400 °C can create oxygen vacancies and active Cu⁰ species as active sites in Cu-CeO₂ catalysts [149]. The SMSI phenomenon allows electrons to move from Cu to Ce on its surface, forming the Ce³⁺-O_v-Cu⁰ and Cu⁰-CeO_{2-δ} interface structures that increase the adsorption and activation of the reactant in RWGS reaction. The results suggested that the Cu-CeO₂ catalyst with 8 wt.% Cu had the best CO₂ conversion yield (Figure 12a). The full synergistic interaction between the active

species via Ce^{3+} -oxygen vacancy- Cu^0 was attributed to its high catalytic activity in the RWGS process [149].

Aitbekova et al. designed the 2.6 nm Ru equally distributed on Al_2O_3 , TiO_2 , and CeO_2 supports and tested in a CO_2 reduction process [55]. Ru catalysts supported on TiO_2 and CeO_2 were significantly more active than those supported on Al_2O_3 , but CH_4 was the predominant product in all cases. Nonetheless, they reported that moderate oxidation of the catalyst at a temperature of 230°C followed by low temperature reduction (230°C), named as OX-LTR, leads to the Ru particles' re-dispersion on CeO_2 , giving a nearly complete switching of product selectivity from methane to CO (Figure 12b), indicating that a weaker adsorption of CO on the single RuO_x site is likely to result in increased selectivity. As they stated in their research, such re-dispersion appears only slightly in Al_2O_3 - and TiO_2 -supported Ru, probably due to the lower Al_2O_3 and TiO_2 and RuO_x interaction as compared to the CeO_2 support with RuO_x . Moreover, a light oxidation of the catalysts at 230°C coupled with a high reduction temperature of 500°C , named as OX-HTR, favored the formation of SMSI in the case of Ru- TiO_2 ; however, the Ru- CeO_2 catalysts (both OX-LTR and OX-HTR) exhibited fairly similar rates, implying the effect of SMSI is negligible for CeO_2 -supported Ru materials under the CO_2 hydrogenation conditions investigated [55]. Similar conclusions were derived by Tauster et al. in a separate study [150].

A capping layer encircling the supported nanoparticles is commonly observed as evidence of the impact [151]. The existence of such an action, on the other hand, could be linked to charge transfer across metallic nanoparticles and the oxide support [152]. For example, Figueiredo et al. synthesized $\text{Cu}_x\text{Ni}_{1-x}\text{-CeO}_2$ ($x = 0.25, 0.35$ and 60) nanoparticles for use in the RWGS reaction and investigated the SMSI influence on CO_2 dissociation reaction by exploring the nanoparticles' electrical and structural features and discovered the reactivity of nanoparticles was proportional to the Cu content on the surface with Cu-richer ones having a negative impact on the CO_2 dissociation reactivity [153]. According to their experimental results, through the reduction treatment, the SMSI effect does not actually impact nanoparticles synthesized with low Cu amounts (Figure 12c). The SMSI situation caused the support's capping layer that surrounds the nanoparticle surface to cover the catalytic active spots on the surface of the nanoparticle, leading to a decrease in the reactivity of CO_2 dissociation [153].

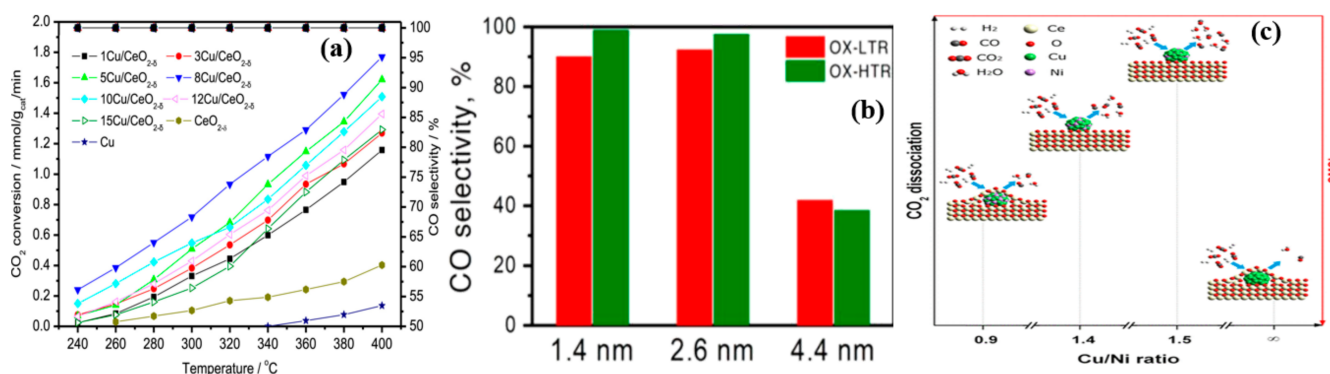


Figure 12. Effect of metal–support interactions on metal- CeO_2 in RWGS reaction: (a) Cu- CeO_2 , reprinted with permission from [149]. Copyright Elsevier, 2020, (b) Ru- CeO_2 , reprinted with permission from [55]. Copyright ACS, 2018, (c) $\text{Cu}_x\text{Ni}_{1-x}\text{-CeO}_2$, reprinted with permission from [153]. Copyright ACS, 2020.

Looking more into the work of Zhou et al., the CO_2 -TPD profiles of the $x\text{Cu}/\text{CeO}_{2.8}$ catalysts are presented in Figure 13, and show two unique CO_2 desorption peaks for each sample [149]. The area of the CO_2 desorption peak and the number of CO_2 adsorption active sites present on the surface of the relevant catalyst are invariably connected. By increasing Cu loading, the peak regions for the ϵ peak exhibited a volcano pattern, reaching their highest on the $8\text{Cu}/\text{CeO}_{2.8}$ catalyst. This was explained in their work by the fact that

increasing Cu loading (8%) led to a greater number of Cu- $\text{CeO}_{2-\delta}$ junctions and encouraged strong MSI. Nonetheless, at larger Cu loadings (>8%), a portion of the surface active sites may be coated by an extreme amount of Cu species [149]. When it comes to the peak ϕ , the peak regions initially start to increase, up to Cu loading of 10%, and then continue to decrease. This was explained by the fact that at lower Cu loadings up to 10%, the catalysts' high specific surface areas enable CO_2 molecules to adsorb on their surfaces, whereas at larger Cu loadings (above 10%), the catalysts' active sites are reduced as a result of the evident decrease in specific surface areas [149].

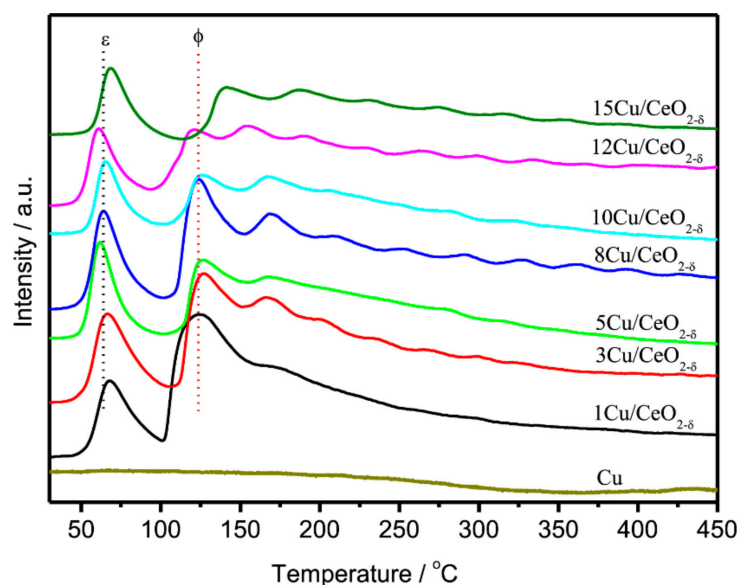


Figure 13. CO_2 -TPD analysis of the Cu/ $\text{CeO}_{2-\delta}$ catalysts, reprinted with permission from [149]. Copyright Elsevier, 2020.

4.4. Active Metal Loading

The influence of the catalysts' composition has been investigated in many studies. Lloret et al. designed catalysts with two different Cu concentrations and two different quantities of ceria precursor, aiming to have two distinct molar ratios of 20Cu:80Ce and 40Cu:60Ce with two different decomposition methods: pyrolysis (P), and PF (Figure 14a) [132]. It was revealed that samples with a higher Cu level have weak catalytic activity, whereas catalysts with a lower Cu content have better catalytic behavior in the RWGS process [132]. It is interesting to note that the ceria crystal size is smaller in the catalyst with higher ceria content (lower Cu), and copper dispersion is reduced when there is a large copper loading. According to the TPR results, hydrogen consumption was higher and peaked at lower temperatures in the sample with less Cu. A high Cu content needed the degradation of a greater quantity of HKUST-1, creating a more reducing environment. Therefore, if higher Cu content is there, additional MOFs are needed to break down to adjust to the reducing environment [132]. The impact of metal nanoparticle concentration on CeO_2 -supported Pt and Ru catalysts with metal contents of 1, 5, and 10% on CeO_2 has been investigated by Einakchi et al. [154]. Comparing Figure 14b,c, raising the metal loading from 1 wt.% to 10 wt.% clearly degrades the activity of Pt catalysts, while it seems to favor the RWGS activity of Ru catalysts. Ru and Pt catalysts are likely to have lower metal dispersion at 10 wt.% when compared to metal loadings of 1 wt.%. The high catalytic performance of Pt- CeO_2 was found to be linked with metal loading and particularly sensitive to metal dispersion, with 1 wt.% Pt displaying the optimum catalytic performance. Unlike Pt- CeO_2 , no correlation was identified between Ru catalyst RWGS activity and metal loading (Ru dispersion); nonetheless, 5 wt.% Ru metal was proven to be the best loading for Ru- CeO_2 catalysts [154]. In another study, Wang et al. prepared Co- CeO_2 catalysts with different cobalt concentrations (0, 1, 2, 5, 10%) using the CP method employed in the RWGS reaction [54]. The findings

revealed that the sample with 2% Co on CeO₂ support showed highly dispersed Co₃O₄ on CeO₂ surface displaying a strong MSI that resulted in an outstanding RWGS catalytic efficiency in terms of activity, CO selectivity, and minimal carbon deposition. Nevertheless, bulk Co₃O₄ with bigger particle size generated in catalysts having high Co content (5% and 10%) lead to considerably higher carbon deposition and enhanced by-product CH₄ generation throughout the process. Their results suggested that for the RWGS reaction, widely dispersed Co which is reduced from highly distributed Co₃O₄ on CeO₂ support, ought to be a major active material, whereas solid Co that has a large particle size could be the main active component for methanation as well as carbon deposition (Figure 14d,e) [54]. The same group in another study investigated the effect of the content of cobalt supported on CeO₂ prepared by a colloidal solution combustion technique to form mesoporous catalysts (Co-CeO₂-M) and examined their activity and selectivity toward RWGS reaction and then compared the optimum Co amount sample with the same catalyst prepared by IM and CP [155]. The catalytic analyses revealed that the mesoporous 5% and 10%Co-CeO₂ catalyst had high activity in the RWGS reaction (Figure 14f); however, 10%Co-CeO₂ was less selective to CO formation than the 5%Co-CeO₂ one. Nonetheless, both had good stability over a 10-h period at 600 °C. Moreover, the activity and selectivity of 5% Co-CeO₂-M was higher than the 5% Co-CeO₂-IM and 5%Co-CeO₂-CP catalysts. They concluded that the superior catalytic performance of the 5%Co-CeO₂-M catalyst was owing to its unique mesoporous configuration, in which the Co particle is dispersed throughout the pore wall and is in close contact to small CeO₂ particles [155]. When defining the optimal catalyst in terms of activity and selectivity, metal dispersion is not the only factor to consider; the nature of the support also plays an important role. According to research by Jurkovic et al. on various supports for Cu-based catalysts, the supports with the greatest Cu dispersion were Al₂O₃ (77.7%) followed by ZrO₂ (73.6%), CeO₂ (67.6%), TiO₂ (66.3%), and SiO₂ (36.2%) [156]. Nevertheless, the alumina support was found to have the highest reported catalytic activity, followed by ceria, titania, silica, and zirconia. Ceria was ranked by TPR as the second-best support among the studied group, while having the third-best Cu dispersion, most likely because of its reducibility and capacity to hold oxygen [156]. Moreover, according to the literature, there is a direct correlation between the catalysts' activity and acid-base properties [157]. According to Pino et al., the synergistic interaction of Ni and La₂O₃ on a La₂O₃ doped Ni-CeO₂ catalyst boosted catalytic activity because of the creation of a basic site and Ni dispersion improvement [158]. Therefore, it can also be concluded that improving basicity of a catalyst might facilitate CO₂ adsorption [74]. According to the research of Jurkovic et al., Al₂O₃ is a frequently used irreducible support with good performance, where its modest acidity could be a likely contributing factor [74,156].

4.5. Metal Size Effect

The RWGS reaction is sensitive to the structure of the supported catalysts, and the size of the attached metal active sites that influence the adsorption, intermediate formation and desorption of the products [159]. Reducing the metal particle size may improve MSI by generating a larger metal-support interface, leading to positively increasing the RWGS reaction activity. Indeed, due to the SMSI effect, more oxygen atoms should be attached to the metal surface when the particle size decreases [160]. For example, Li et al. developed a 5% Ir-CeO₂ catalyst including an Ir particle size of around 1 nm, and a 0.7% Ir-CeO₂ catalyst with atomic dispersion of Ir [161]. Even though the dominant product of CH₄ was produced by an Ir-CeO₂ catalyst with large Ir particles (>2.5 nm), CO was produced mainly by the 5% and 0.7% Ir-CeO₂ catalysts when Ir particle size was less than 1 nm, and the catalytic activity per mole of Ir increased (Figure 15a). They also discovered that due of the intense interaction with CeO₂, 1 nm Ir particles and atomically dispersed Ir get partially oxidized, but large Ir particles, more than 2.5 nm, are mostly reduced. As a result, they concluded that the primary active site for a RWGS reaction is partly oxidized Ir that engages extensively with CeO₂ support regardless of Ir particles or atomically dispersed Ir atoms [161]. Metal active sites distributed on an atomic level add more to the

CO product than metal clusters at a 3D level [162]. In a study, Zhao et al. produced Pt-CeO₂ catalysts with various Pt sizes to test the influence of size on CO selectivity in the RWGS reaction [163]. Three Pt-CeO₂ catalysts were produced using CeO₂ nanorods, including atomically dispersed Pt species as well as Pt clusters or particles of two different sizes (2.1 and 5.2). According to Figure 15 b, within the temperature range of 200 to 450 °C, the atomically distributed Pt-CeO₂ catalyst (shown as Pt-CeO₂-AA-350) exhibited almost 100% CO selectivity, whereas CO selectivity using Pt nanoparticles (5Pt-CeO₂-IMP-350 catalyst with 5.2 nm particle size) reduced noticeably at elevated reaction temperature. Large-sized Pt species demonstrated high CO adsorption, resulting in the production of CH₄ by further hydrogenation [163].

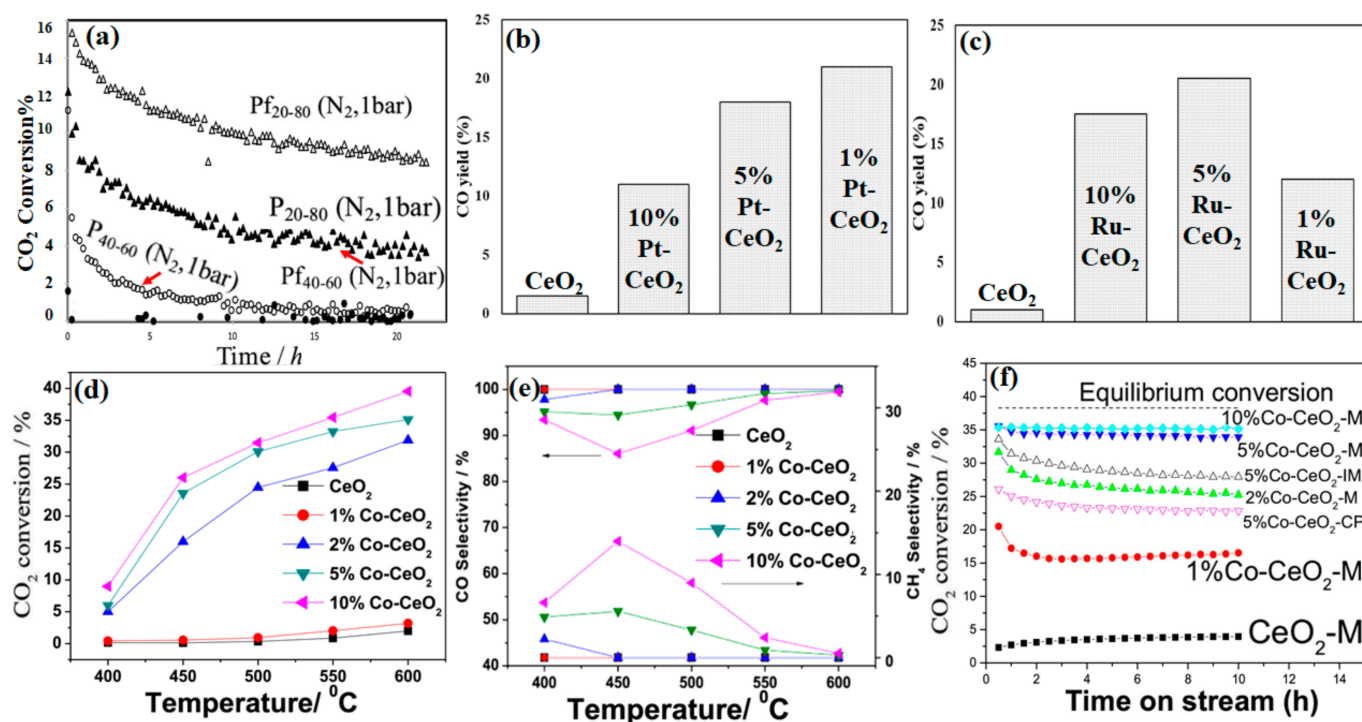


Figure 14. Effect of metal loading on metal-CeO₂ RWGS reaction: (a) CuO_x-CeO₂, adapted with permission from [132]. Copyright Elsevier, 2018, (b,c) CO yield at 450 °C, (b) Pt-CeO₂, (c) Ru-CeO₂, (d,e) activity and selectivity of Co-CeO₂, reprinted with permission from [54]. Copyright Elsevier, 2017, (f) Co-CeO₂, reprinted with permission from [155]. Copyright Elsevier, 2018.

Lu et al. developed mesoporous CeO₂ (surface area = 100 m² g^{−1}) as well as NiO-CeO₂ with large surface areas, narrow pore size dispersion, and homogeneous mesopores (intercrystallite voids) [53]. According to the results, with increasing temperature and NiO quantity, the CO₂ conversion rate in RWGS reaction increased. As for CO selectivity, when less than 3 wt.% NiO was used, NiO particles monodispersed in mesoporous CeO₂ resulting in a complete CO₂ conversion to CO which was irrespective of temperature. For more than 3.5 wt.%, due to NiO particle aggregation, 100% CO selectivity was improbable below 700 °C (Figure 15c) [53]. Wang et al. studied the effect of CeO₂ on RWGS in comparison to In₂O₃ [164]. The surface areas of the In₂O₃-CeO₂ catalysts enhanced compared to pure In₂O₃; as the CeO₂ content increased, the size of the In₂O₃ particles in the In₂O₃-CeO₂ samples reduced and the dispersion of In₂O₃ particles in the In₂O₃-CeO₂ increased. Besides, additional oxygen vacancies were formed (Figure 15d), which in turn enhanced the dissociative hydrogen adsorption and increased the quantity of bicarbonate species produced by activated CO₂ adsorption [164].

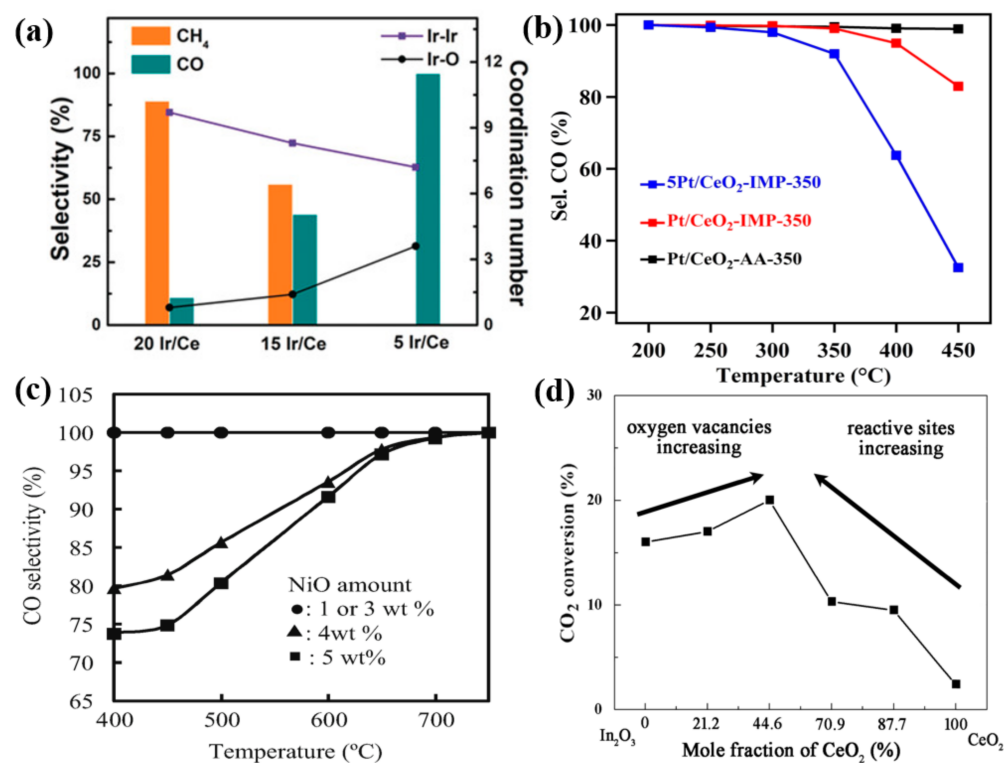


Figure 15. Effect of metal size CeO₂ support on RWGS reaction: (a) Ir-CeO₂, reprinted with permission from [161], Copyright Wiley, 2017, (b) Pt-CeO₂, reprinted with permission from [163]. Copyright Elsevier, 2021, (c) NiO-CeO₂, reprinted with permission from [53]. Copyright Elsevier, 2014, (d) In₂O₃-CeO₂, reprinted with permission from [164]. Copyright Elsevier, 2016.

4.6. Effect of Adding CeO₂ as a Reducible Transition Metal Oxide Promoter

The inclusion of a cerium oxide as a promoter can affect CO₂ adsorption and activation, as well as the activity and selectivity of the RWGS process [165,166]. Yang et al. showed in their work how adding ceria to alumina support (CeO₂-Al₂O₃) helped in lowering acidity of Ni-based catalysts, which also minimized carbon deposition [167]. Figure 10a shows the catalytic performance of all samples versus temperature in terms of CO₂ conversion. Moreover, introduction CeO₂ to the unpromoted Ni-Al catalyst also improved its reducibility. As it is shown in Figure 16a, ceria improved unpromoted Ni-Al catalyst reducibility in that the Ni-CeAl catalyst had a reduction percentage (RP) of ~93%, compared to 86.5% for the reference Ni-Al catalyst. The authors concluded that their findings were mostly due to two aspects occurring together: (1) CeO₂, as a promoter here, reduced the Ni-Al₂O₃ connection, leading to an increase in Ni particle reducibility, owing to the generated Ni-promoter interaction, and (2) because of its intrinsic redox capabilities, CeO₂ offered additional oxygen mobility to the catalysts [96]. In another study by Lee et al., a set of Pt-CeO₂-TiO₂ catalysts were impregnated with different support combinations ranging from 0 to 20% to evaluate the influence of varied CeO₂/TiO₂ ratio on catalytic activity during RWGS reaction [82]. Accordingly (Figure 16b), increasing CeO₂ loading improved the catalytic activity of Pt-impregnated catalysts, the Pt-20%CeO₂-TiO₂ sample showing the highest CO₂ conversion. Based on their analysis, by substituting TiO₂ with CeO₂, the lattice and pore configuration changed in favor of more CO₂ conversion in RWGS reaction (the mechanism is explained in Figure 3b) [82]. With the aim of improving adsorption and activation of CO₂ on Ga₂O₃, Zhao et al. used CeO₂ as a promoter with an optimum Ga:Ce ratio of 99:1 and employed RWGS reaction as a test reaction and indicator for the catalytic performance of the resultant samples [99]. The results showed the positive performance of CeO₂-Ga₂O₃ (Figure 16c) due to the fact that the inclusion of CeO₂ increases the production of bicarbonate species in CO₂ adsorption, which is thermodynamically

more advantageous [99]. The same catalytic system was studied by Dai et al., where the gel sol-gel process was used to create a variety of Ga_2O_3 - CeO_2 composite oxide catalysts with various Ga_2O_3 and CeO_2 ratios [90]. When compared to pure Ga_2O_3 and pure CeO_2 , the composite oxide catalysts had smaller particles and showed high CO selectivity in the RWGS process. It was discovered that Ga_2O_3 has distinct reaction intermediates from CeO_2 and Ga_2O_3 - CeO_2 , making it easier to create methane in high H_2 conditions, whereas CeO_2 promotes CO selectivity. In a Ga_2O_3 to CeO_2 ratio of 3:1, composite oxide showed the greatest activity (Figure 16d). This is mostly due to the creation of the $\text{Ga}_x\text{Ce}_y\text{O}_z$ solid solution phase and the development of additional active sites that result in an increased number of oxygen vacancies, which facilitate CO_2 adsorption and activation. Moreover, it was found that GaCe composite oxides have a more homogeneous mesoporous structure and a greater pore volume, making mass transport in reactions easier [90]. In contrast, there are a few cases in which once ceria was introduced to a catalytic system, CO selectivity improved but CO_2 conversion was slightly decreased [168]. Galvita et al., for example, developed a Fe_2O_3 - CeO_2 composite and discovered that incorporating ceria to iron oxide increased solid solution stability but reduced CO production capabilities [169].

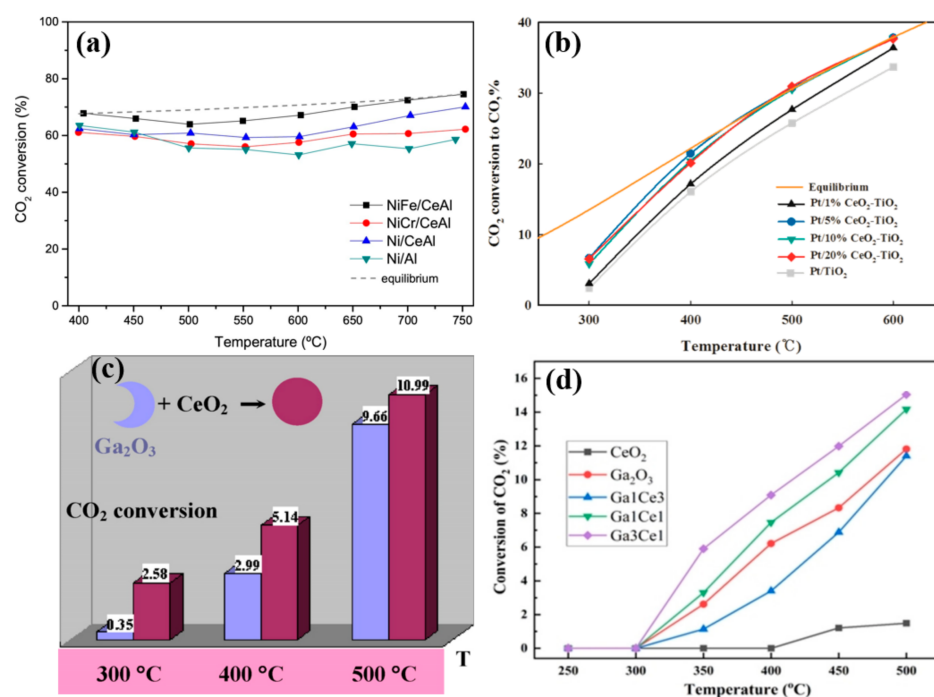


Figure 16. Effect of adding promoters on RWGS reaction: (a) Ni-CeAl, reprinted with permission from [167]. Copyright Elsevier, 2018, (b) Pt-CeTi at 400 °C, (c) CeO_2 - Ga_2O_3 , reprinted with permission from [99]. Copyright Elsevier, 2012, (d) Ga_2O_3 - CeO_2 , reprinted with permission from [90]. Copyright Wiley, 2022.

On the other hand, when a non-reducible transition metal oxide is used as a promoter for M- CeO_2 catalysts, more oxygen vacancies can emerge during the reduction process [170]. For example, more thermally stable support can be developed by a mixed framework of Al_2O_3 - CeO_2 which offers a broad surface for optimum active phase dispersion and enables the development of oxygen vacancies on the surface throughout the catalytic reaction to improve catalytic performance [171]. Zonetti et al. and Wenzel et al. showed that adding Zr to the CeO_2 lattice improved its ability to create oxygen vacancies as well as its thermal stability, which is a desirable feature of catalytic systems [172,173].

4.7. Bimetallic Effect

Reports indicate that bimetals, where a second metal is introduced along with the primary active metal, can be used to help boost the catalytically active phase [174]. Evi-

dently in many systems, bimetallic compounds have outperformed their individual components [175]. Furthermore, the generation of metal carbide (coke precursor) could be prevented due to the electrical effect caused by metal–metal interactions, resulting in less deactivation [176]. Yang et al. showed how the inclusion of a second element (Cr or Fe) can positively affect the reducibility of monometallic Ni-based catalysts (Ni–CeAl) [167]. As it is displayed in Figure 17a, the addition of Fe to the Ni–CeAl catalyst system can increase the reducibility of Ni- to 95% compared to 93% for the Ni–CeAl catalyst [167]. Chen et al. synthesized a Cu–Fe bimetallic phase loaded on CeO₂ and evaluated its performance for RWGS reaction at temperatures ranging from 450 to 750 °C at 1 atm (Figure 17b). The efficiency of the iron-containing copper-based catalyst was greatly increased over that of the catalyst without iron, and CO₂ conversion nearly approached theoretical levels. The bimetallic CeO₂-supported catalyst was shown to have high selectivity, stability, with no secondary reactions, and no carbon deposition on the catalyst surface after the process [177]. In contrast, Li et al. used CuIn bimetallic catalysts for the RWGS reaction, demonstrating that the promotional impact of In on Cu is support dependent [91]. The CO₂ conversion of the CuIn–ZrO₂ catalyst was higher by far than the Cu–ZrO₂ catalyst; however, the CO₂ conversion of CuIn–CeO₂ was considerably lower than Cu–CeO₂ (Figure 17c). The cause of the support-sensitivity of RWGS activity was further discovered through systematic analysis. Cu and In combined to form CuIn alloys on the ZrO₂ support, which allowed CO₂ to be activated by oxygen vacancies from partially reduced In₂O₃, whereas, Cu and In were found as metallic Cu and In₂O₃ on the CeO₂ support, respectively. The addition of In prevented Cu dispersion and the development of oxygen vacancies on CeO₂, resulting in lower RWGS activity [91]. The catalytic activity of 5 wt.% mono- and bimetallic Ru- and Pt-based catalysts supported on CeO₂ was compared as a function of temperature as shown in Figure 17d [154]. The bimetallic activity is higher than that of the individual Ru activities due to the synergy between Ru, Pt, and CeO₂. Moreover, the Fe-promotional impact in the Ru₉₀Fe₁₀–CeO₂ catalyst is most noticeable at lower temperatures, whereas there is no difference in catalytic activity above 450 °C when compared to Ru–CeO₂ [154].

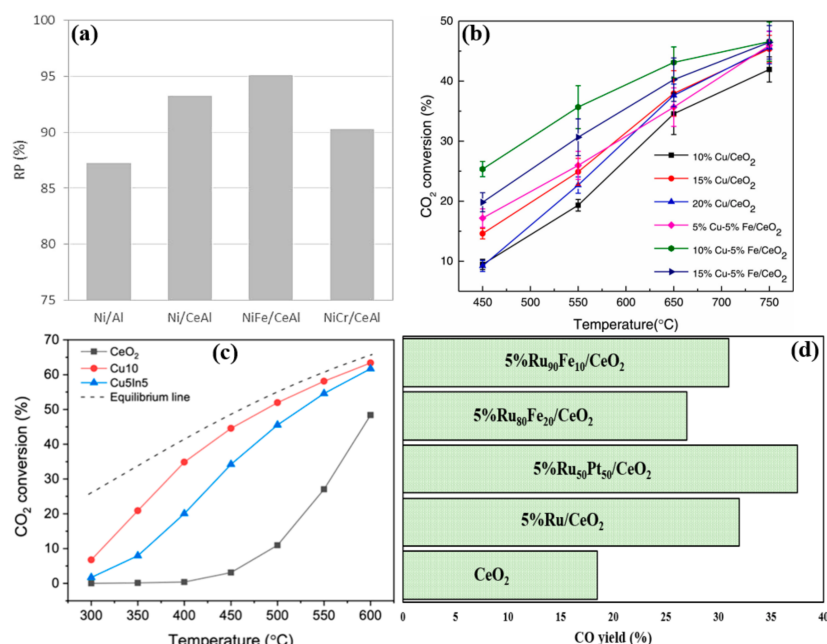


Figure 17. Effect of bimetallic on metal–CeO₂ in RWGS reaction: (a) NiFe–CeO₂, reprinted with permission from [167]. Copyright Elsevier, 2018, (b) CuFe–CeO₂, reprinted with permission from [177]. Copyright Elsevier, 2021, (c) CuIn–CeO₂, reprinted with permission from [91]. Copyright ACS, 2022, (d) CO yield for RuPt/CeO₂ and RuFe/CeO₂ at 600 °C.

The following table (Table 3) provides a summary of M-CeO₂ catalysts used in RWGS reaction. The synthesis methods and relevant results are provided for comparing their performance.

Table 3. Conditions and catalytic performance in RWGS reaction on different kinds of metal-CeO₂.

Catalyst	Synthesizing Method	Temperature (°C)	Conversion (%)	Selectivity (%)	Ref.
Pt-CeO ₂	Co-Precipitation	300	6.7	-	[94]
2%Pt-CeO ₂	Commercial	290	21.7	~100	[178]
1 wt.%Pt-CeO ₂	Polyol	500	~24	~100	[154]
3.2%PtCo-CeO ₂	Incipient Wetness Impregnation	300	9.1	92.3	[179]
5 wt.%Ru-CeO ₂	Polyol	500	~25	~100	[154]
5%Ru-CeO ₂	Polyol	350	~16	~31	[180]
Ru50Pt50-CeO ₂	Polyol	500	~28	~100	[154]
RuNi-CeZ	Wet Impregnation	350	53	93	[181]
5%Ru/Sm-CeO ₂	Polyol	350	~16	~69	[180]
FeNi-CeZr	Wet Impregnation	350	13	60	[181]
PtCo-CeO ₂	Incipient Wetness Impregnation	300	9.1	92.31	[179]
0.5Pd10Cu-CeO ₂	Precipitation–Impregnation	270	12	-	[182]
1Pd10Cu-CeO ₂	Precipitation–Impregnation	270	17.8	-	[182]
2Pd10Cu-CeO ₂	Precipitation–Impregnation	270	11.3	-	[182]
PdNi-CeO ₂	Incipient Wetness Impregnation	300	2.5	37.5	[183]
10Cu-CeO ₂	Precipitation–Impregnation	270	6.4	-	[182]
Cu-CeO ₂	Space-Confined	300	~18	~100	[184]
CeO ₂ -NC	Hydrothermal–Incipient Wetness Impregnation	700	27.8	~100	[83]
CeO ₂ -NR	Hydrothermal–Incipient Wetness Impregnation	700	23.8	~100	[83]
CeO ₂ -NO	Hydrothermal–Incipient Wetness Impregnation	700	19.8	~100	[83]
CeO ₂ -HT	Hard-Template	580	15.9	~100	[131]
Cu/CeO ₂	Wet Impregnation	380	52	95	[140]
CuCeO _x	Hard Template	400	33	~100	[51]
CuO _x -CeO ₂	Wet Impregnation	400	10	~100	[132]
1 wt.%Cu-CeO ₂	Combustion	600	~70	~100	[28]
5.60 wt.%Cu-CeO ₂ -hs	Hydrothermal–Impregnation	600	~50	~100	[88]
5 wt.%Cu-CeO ₂ -nr	Hydrothermal–incipient wetness impregnation	450	~50	-	[81]
5 wt.%Cu-CeO ₂ -ns	Microemulsion–incipient wetness impregnation	450	~40	-	[81]
0.25 mole%Cu-CeO ₂	Hard Template–Impregnation	400	31.34	100	[185]
5Cu/48CeO ₂ /ZSM	Physical Mixing	600	~68	100	[186]
Fe-CeO ₂	Hard Template–Impregnation	340	3.3	~100	[185]
Mn-CeO ₂	Hard Template–Impregnation	340	3.3	~100	[128]
Co-CeO ₂	Hard Template–Impregnation	340	9.3	~100	[128]
10%Co-CeO ₂	Colloidal Solution Combustion	300	3.8	39.4	[155]
10Cu5Fe-CeO ₂	Impregnation	750	42	100	[177]
5Cu5In-CeO ₂	Impregnation	500	45	100	[91]
10Cu-CeO ₂	Impregnation	500	50	100	[91]
10 wt.%Co-CeO ₂	Co-precipitation–Impregnation	500	28	~91	[187]
1%K10% Co-CeO ₂	Co-precipitation–Impregnation	500	31	100	[187]
1%Ni-CeO ₂	Co-precipitation	600	~35	100	[188]
1%Ni-CeO ₂	Co-precipitation	400	~4.5	~90	[130]
Ni-CeO ₂	Co-precipitation	700	37.5	~100	[121]
Ni-CeO ₂	Deposition–Precipitation	700	41.7	~100	[121]
Ni-CeO ₂	Impregnation	700	29.2	~100	[121]
Ni-CeZrO _x	Impregnation	700	46.1	97.3	[189]
Ni/CeO ₂ -Al ₂ O ₃	Wet Impregnation	750	59	94	[167]
Ni-CeZrO _x	Precipitation–Co-precipitation	550	48	87.5	[172]
1%NiO-CeO ₂ /SBA-15	Calcination	450	~2.5	100	[53]
6%Ni/Al ₂ O ₃ -CeO ₂	Combustion	750	~63	~90	[190]
RuFe-CeO ₂	Polyol	800	47.5	~100	[180]
0.7%Ir-CeO ₂	Adsorption–Precipitation	300	2.9	>99	[161]
5%Ir-CeO ₂	Adsorption–Precipitation	300	6.8	>99	[161]
20%Ir-CeO ₂	Adsorption–Precipitation	300	8.8	12	[161]
In ₂ O ₃ -CeO ₂	Co-precipitation	500	20.4	~100	[164]
Ga ₂ O ₃ -CeO ₂	Physical Mixing	400	5.14	~100	[99]

5. Summary and Outlook

The RWGS is a potential process with a promising prospect for large-scale CO₂ to CO conversion in the near future, when integrated with large-scale technologies for sustainable H₂ production. If the RWGS reaction is to play a significant role in lowering CO₂ levels in the atmosphere, a suitable catalyst made of earth-abundant elements is desirable. CeO₂ support has been shown to aid in increasing CO₂ catalytic activity, and the following key features make CeO₂ an attractive choice:

- CeO₂ supports are renowned for their acid-base properties, and high oxygen mobility and stability, which improve RWGS reaction activity when added to a suitable active metal catalytic system.
- Surface defects (Ce³⁺ and oxygen vacancies) enable metal particles to attach well to the ceria support, resulting in increased metal dispersion.
- A Ce⁴⁺/Ce³⁺ redox pair with strong activity can significantly improve CO₂ dissociative activation.
- Sintering processes and coke formation may be hampered by a strong metal–support interaction (MSI) leading to an enhancement in catalyst stability.
- CeO₂ can be produced by a variety of methods to provide suitable design and technical features generating appropriate metal–support interactions that can further be tuned by synthesis methods and catalyst pretreatment techniques.
- CeO₂ support could influence the reaction mechanism by changing the adsorption energy of key intermediates with MSI.

The mechanism of the RWGS reaction involving CeO₂ as a support, as well as an active site, have been thoroughly debated, since understanding these concepts is critical for the rational design of highly efficient and selective RWGS catalysts. Although the RWGS reaction mechanism is still a controversial topic, the reaction routes on different catalysts working under different reaction parameters may be clarified in the near future due to the advancements in *in situ* and *operando* spectroscopic technologies, including *in situ* (*or near ambient pressure* (NAP)) XPS and *in situ* XRD, in combination with theoretical approaches involving DFT. Identifying the deactivation pathway may also help in the development of stable catalysts for the RWGS reaction.

In this context, developing a more structurally and thermally stable CeO₂ that can achieve high CO selectivity at high CO₂ conversion rates with less carbon deposition to prevent catalyst deactivation is critical. A careful approach is needed to develop and activate CeO₂ based catalysts and fine-tune their properties by regulating MSI to generate the desired effects. The literature shows the implementation of a range of parameters that influence CeO₂ catalyst performance in RWGS reaction, such as the addition of a suitable second metal in bimetallic systems, adaptation of apt catalyst preparation methods to optimize active metal size, addition of CeO₂ as a promoter for metal-supported catalysts, tuning CeO₂ crystal planes for oxide catalysts etc. Recently, transition metal carbides have been seen as an appealing and suitable option for commercial applications in the RWGS reaction due to their interesting features comparable to those of noble metals such as their dual capabilities for H₂ dissociation and C–O bond regulation, and possibility to act similarly to reducible oxides. Even though numerous materials have been investigated, no commercial-scale catalyst is available for RWGS reaction and further progress and scientific understanding is required before an industrial level of implementation can be thought of. So far, only a few studies are available on the kinetic model and reaction rate determination on M–CeO₂ catalysts in RWGS reaction, and more dedicated future studies are required to fulfill this critical gap; it is necessary to expand this study further, to reactor development and large-scale expansion. The engineering of an industrial RWGS unit requires a comprehensive knowledge of reaction kinetics, involving internal/external mass transport impacts, along with the RWGS thermodynamic equilibrium.

Author Contributions: Conceptualization, P.E. and A.K.; methodology, P.E. and A.K.; writing—original draft preparation, P.E.; writing—review and editing, A.K. and M.K.; supervision, A.K. and M.K.; project administration, A.K.; funding acquisition, A.K. and M.K. All authors have read and agreed to the published version of the manuscript.

Funding: This research was funded by Qatar National Research Fund, grant number NPRP8-509-2-209 and NPRP10-0107-170119.

Data Availability Statement: Not applicable.

Acknowledgments: The work was made possible by a grant from the Qatar National Research Fund under the National Priorities Research Program award numbers NPRP8-509-2-209 and NPRP10-0107-170119. Its contents are solely the responsibility of the authors and do not necessarily represent the official views of QNRF. The authors would also like to gratefully acknowledge the support of Graduate Teaching/Research Assistantship (GTRA) from Qatar University in conducting this research.

Conflicts of Interest: The authors declare no conflict of interest.

Abbreviations

ABC	Artificial Bee Colony
ALE	Atomic Layer Epitaxy
BET	Brunauer–Emmett–Teller
CA	Complex
CP	Co-Precipitation
DE	Differential Evolution
DFT	Density Functional Theory
DP	Deposition-Precipitation
DRIFTS	Diffuse Reflectance Infrared Fourier-Transform Spectroscopy
EDX	Energy Dispersive X-ray
FCC	Face-Centered Cubic
FTS	Fischer–Tropsch Synthesis
HT	Hard-template
HTR	High Temperature Reduction
IM	Impregnation
LHHW	Langmuir–Hinshelwood–Hougen–Watson
LN	Liquid Nitrogen
LSPR	Localized Surface Plasmon Resonance
LTR	Low Temperature Reduction
M	Mesoporous
MOF	Metal Organic Framework
MSI	Metal–Support Interaction
NAP	Near Ambient Pressure
NC	Nanocube
NO	Nanooctahedra
NR	Nanorod
NS	Nanospheres
OSC	Oxygen Storage Capacity
OX	Oxidation
P	Pyrolysis
PC	Precipitation
PF	Flash Pyrolyzed
RDS	Rate-Determining Step
RM	Reverse Microemulsion
RP	Reduction Percentage
RWGS	Reverse Water Gas Shift
SEM	Scanning Electron Microscopy
SMSI	Strong Metal–Support Interaction
TEM	Transmission Electron Microscopy
TPR	Temperature Programmed Reduction

WGS	Water Gas Shift
WI	Wet Impregnation
XPS	X-ray Photoelectron Spectroscopy
XRD	X-ray Diffraction

References

- Yang, X.; Su, X.; Chen, X.; Duan, H.; Liang, B.; Liu, Q.; Liu, X.; Ren, Y.; Huang, Y.; Zhang, T. Promotion effects of potassium on the activity and selectivity of Pt/zeolite catalysts for reverse water gas shift reaction. *Appl. Catal. B Environ.* **2017**, *216*, 95–105. [\[CrossRef\]](#)
- Ebrahimi, P.; Kumar, A.; Khraisheh, M. Thermodynamic assessment of effect of ammonia, hydrazine and urea on water gas shift reaction. *Int. J. Hydrogen Energy* **2020**, *47*, 3237–3247. [\[CrossRef\]](#)
- Sasol ECOFT and Deutsche Aircraft join forces to accelerate power-to-liquid (PTL) aiming for carbon-neutral flight. *Focus Catal.* **2022**, *2022*, 4. [\[CrossRef\]](#)
- Liu, X.; Pajares, A.; Matienzo, D.D.C.; de la Piscina, P.R.; Homs, N. Preparation and characterization of bulk MoXC catalysts and their use in the reverse water-gas shift reaction. *Catal. Today* **2020**, *356*, 384–389. [\[CrossRef\]](#)
- Centi, G.; Perathoner, S. Opportunities and prospects in the chemical recycling of carbon dioxide to fuels. *Catal. Today* **2009**, *148*, 191–205. [\[CrossRef\]](#)
- Aresta, M. *Carbon Dioxide as Chemical Feedstock*; John Wiley & Sons: Hoboken, NJ, USA, 2010.
- Ueckerdt, F.; Bauer, C.; Dirnau, A.; Everall, J.; Sacchi, R.; Luderer, G. Potential and risks of hydrogen-based e-fuels in climate change mitigation. *Nat. Clim. Chang.* **2021**, *11*, 384–393. [\[CrossRef\]](#)
- Olah, G.A.; Goeppert, A.; Prakash, G.S. Chemical recycling of carbon dioxide to methanol and dimethyl ether: From greenhouse gas to renewable, environmentally carbon neutral fuels and synthetic hydrocarbons. *J. Org. Chem.* **2009**, *74*, 487–498. [\[CrossRef\]](#)
- Sterner, M. *Bioenergy and Renewable Power Methane in Integrated 100% Renewable Energy Systems. Limiting Global Warming by Transforming Energy Systems: Limiting Global Warming by Transforming Energy Systems*; Kassel University Press GmbH: Hesse, Germany, 2009; Volume 14.
- Pastor-Pérez, L.; Baibars, F.; Le Sache, E.; Arellano-Garcia, H.; Gu, S.; Reina, T.R. CO₂ valorisation via reverse water-gas shift reaction using advanced Cs doped Fe-Cu/Al₂O₃ catalysts. *J. CO₂ Util.* **2017**, *21*, 423–428. [\[CrossRef\]](#)
- Galván, C.Á.; Schumann, J.; Behrens, M.; Fierro, J.L.G.; Schlögl, R.; Frei, E. Reverse water-gas shift reaction at the Cu/ZnO interface: Influence of the Cu/Zn ratio on structure-activity correlations. *Appl. Catal. B Environ.* **2016**, *195*, 104–111. [\[CrossRef\]](#)
- Sheehan, S.W. Electrochemical methane production from CO₂ for orbital and interplanetary refueling. *Iscience* **2021**, *24*, 102230. [\[CrossRef\]](#)
- Xu, X.D.; Moulijn, J.A. Mitigation of CO₂ by chemical conversion: Plausible chemical reactions and promising products. *Energy Fuels* **1996**, *10*, 305–325.
- Kwak, J.H.; Kovarik, L.; Szanyi, J.N. Heterogeneous catalysis on atomically dispersed supported metals: CO₂ reduction on multifunctional Pd catalysts. *ACS Catal.* **2013**, *3*, 2094–2100. [\[CrossRef\]](#)
- Yasuda, T.; Uchiage, E.; Fujitani, T.; Tominaga, K.-I.; Nishida, M. Reverse water gas shift reaction using supported ionic liquid phase catalysts. *Appl. Catal. B Environ.* **2018**, *232*, 299–305. [\[CrossRef\]](#)
- Wender, I. Reactions of synthesis gas. *Fuel Process. Technol.* **1996**, *48*, 189–297. [\[CrossRef\]](#)
- ExxonMobil unveils tech for methanol-to-SAF. *Focus Catal.* **2022**, *2022*, 6. [\[CrossRef\]](#)
- Kumar, A.; Mohammed, A.A.; Saad, M.A.; Al-Marri, M.J. Effect of nickel on combustion synthesized copper/fumed-SiO₂ catalyst for selective reduction of CO₂ to CO. *Int. J. Energy Res.* **2022**, *46*, 441–451. [\[CrossRef\]](#)
- De Miranda, P.E.V. Chapter 5.3.3—Application of Hydrogen by Use of Chemical Reactions of Hydrogen and Carbon Dioxide. In *Science and Engineering of Hydrogen-Based Energy Technologies*; de Miranda, P.E.V., Ed.; Academic Press: Cambridge, MA, USA, 2019; pp. 279–289.
- Stangeland, K.; Kalai, D.; Li, H.; Yu, Z. CO₂ methanation: The effect of catalysts and reaction conditions. *Energy Procedia* **2017**, *105*, 2022–2027. [\[CrossRef\]](#)
- Nityashree, N.; Price, C.; Pastor-Perez, L.; Manohara, G.; Garcia, S.; Maroto-Valer, M.M.; Reina, T. Carbon stabilised saponite supported transition metal-alloy catalysts for chemical CO₂ utilisation via reverse water-gas shift reaction. *Appl. Catal. B Environ.* **2020**, *261*, 118241. [\[CrossRef\]](#)
- Dias, Y.R.; Perez-Lopez, O.W. Carbon dioxide methanation over Ni-Cu/SiO₂ catalysts. *Energy Convers. Manage.* **2020**, *203*, 112214. [\[CrossRef\]](#)
- Elsernagawy, O.Y.; Hoadley, A.; Patel, J.; Bhatelia, T.; Lim, S.; Haque, N. Thermo-economic analysis of reverse water-gas shift process with different temperatures for green methanol production as a hydrogen carrier. *J. CO₂ Util.* **2020**, *41*, 101280. [\[CrossRef\]](#)
- Kaiser, P.; Unde, R.B.; Kern, C.; Jess, A. Production of liquid hydrocarbons with CO₂ as carbon source based on reverse water-gas shift and Fischer-Tropsch synthesis. *Chem. Ing. Tech.* **2013**, *85*, 489–499. [\[CrossRef\]](#)
- York, A.P.; Xiao, T.C.; Green, M.L.; Claridge, J.B. Methane oxyforming for synthesis gas production. *Catal. Rev.* **2007**, *49*, 511–560. [\[CrossRef\]](#)
- Unde, R.B. *Kinetics and Reaction Engineering Aspects of Syngas Production by the Heterogeneously Catalysed Reverse Water Gas Shift Reaction*; Universitaet Bayreuth: Bayreuth, Germany, 2012.

27. Wu, H.; Chang, Y.; Wu, J.; Lin, J.; Lin, I.; Chen, C. Methanation of CO₂ and reverse water gas shift reactions on Ni/SiO₂ catalysts: The influence of particle size on selectivity and reaction pathway. *Catal. Sci. Technol.* **2015**, *5*, 4154–4163. [\[CrossRef\]](#)
28. Ebrahimi, P.; Kumar, A.; Khraisheh, M. Combustion synthesis of copper ceria solid solution for CO₂ conversion to CO via reverse water gas shift reaction. *Int. J. Hydrogen Energy* **2022**, *in press*. [\[CrossRef\]](#)
29. Ammal, S.C.; Heyden, A. Origin of the unique activity of Pt/TiO₂ catalysts for the water–gas shift reaction. *J. Catal.* **2013**, *306*, 78–90. [\[CrossRef\]](#)
30. Ebrahimi, P.; Kumar, A.; Khraisheh, M. A review of recent advances in water–gas shift catalysis for hydrogen production. *Emergent Mater.* **2020**, *3*, 881–917. [\[CrossRef\]](#)
31. Boaro, M.; Colussi, S.; Trovarelli, A. Ceria-based materials in hydrogenation and reforming reactions for CO₂ valorization. *Front. Chem.* **2019**, *7*, 28. [\[CrossRef\]](#)
32. Ebrahimi, P.; Kumar, A.; Khraisheh, M. Analysis of combustion synthesis method for Cu/CeO₂ synthesis by integrating thermodynamics and design of experiments approach. *Results Eng.* **2022**, *15*, 100574. [\[CrossRef\]](#)
33. Ishito, N.; Hara, K.; Nakajima, K.; Fukuoka, A. Selective synthesis of carbon monoxide via formates in reverse water–gas shift reaction over alumina-supported gold catalyst. *J. Energy Chem.* **2016**, *25*, 306–310. [\[CrossRef\]](#)
34. Trovarelli, A. Catalytic properties of ceria and CeO₂-containing materials. *Catal. Rev.* **1996**, *38*, 439–520. [\[CrossRef\]](#)
35. Yeung, C.M.; Tsang, S.C. A study of co-precipitated bimetallic gold catalysts for water–gas shift reaction. *Catal. Commun.* **2008**, *9*, 1551–1557.
36. Chang, K.; Zhang, H.; Cheng, M.-J.; Lu, Q. Application of ceria in CO₂ conversion catalysis. *ACS Catal.* **2019**, *10*, 613–631. [\[CrossRef\]](#)
37. Castaño, M.G.; Reina, T.R.; Ivanova, S.; Centeno, M.; Odriozola, J.A. Pt vs. Au in water–gas shift reaction. *J. Catal.* **2014**, *314*, 1–9. [\[CrossRef\]](#)
38. Moreira, M.N.; Ribeiro, A.M.; Cunha, A.F.; Rodrigues, A.E.; Zabilskiy, M.; Djinoić, P.; Pintar, A. Copper based materials for water–gas shift equilibrium displacement. *Appl. Catal. B Environ.* **2016**, *189*, 199–209. [\[CrossRef\]](#)
39. Porosoff, M.D.; Chen, J.G. Trends in the catalytic reduction of CO₂ by hydrogen over supported monometallic and bimetallic catalysts. *J. Catal.* **2013**, *301*, 30–37. [\[CrossRef\]](#)
40. Younis, A.; Chu, D.; Li, S. Cerium oxide nanostructures and their applications. *Funct. Nanomater.* **2016**, *3*, 53–68.
41. Yao, S.; Xu, W.; Johnston-Peck, A.; Zhao, F.; Liu, Z.; Luo, S.; Senanayake, S.; Martínez-Arias, A.; Liu, W.; Rodriguez, J. Morphological effects of the nanostructured ceria support on the activity and stability of CuO/CeO₂ catalysts for the water–gas shift reaction. *PCCP* **2014**, *16*, 17183–17195. [\[CrossRef\]](#)
42. Sayle, D.C.; Maicananu, S.A.; Watson, G.W. Atomistic models for CeO₂ (111), (110), and (100) nanoparticles, supported on yttrium-stabilized zirconia. *J. Am. Chem. Soc.* **2002**, *124*, 11429–11439. [\[CrossRef\]](#)
43. Jiang, Y.; Adams, J.B.; Van Schilfgaarde, M. Density-functional calculation of CeO₂ surfaces and prediction of effects of oxygen partial pressure and temperature on stabilities. *J. Chem. Phys.* **2005**, *123*, 064701. [\[CrossRef\]](#)
44. Chen, Y.; Hu, P.; Lee, M.-H.; Wang, H. Au on (1 1 1) and (1 1 0) surfaces of CeO₂: A density-functional theory study. *Surf. Sci.* **2008**, *602*, 1736–1741. [\[CrossRef\]](#)
45. Sayle, T.X.; Cantoni, M.; Bhatta, U.M.; Parker, S.C.; Hall, S.R.; Möbus, G.; Molinari, M.; Reid, D.; Seal, S.; Sayle, D.C. Strain and architecture-tuned reactivity in ceria nanostructures; enhanced catalytic oxidation of CO to CO₂. *Chem. Mater.* **2012**, *24*, 1811–1821. [\[CrossRef\]](#)
46. Liu, X.; Zhou, K.; Wang, L.; Wang, B.; Li, Y. Oxygen vacancy clusters promoting reducibility and activity of ceria nanorods. *J. Am. Chem. Soc.* **2009**, *131*, 3140–3141. [\[CrossRef\]](#) [\[PubMed\]](#)
47. Si, R.; Flytzani-Stephanopoulos, M. Shape and crystal-plane effects of nanoscale ceria on the activity of Au–CeO₂ catalysts for the water–gas shift reaction. *Angew. Chem.* **2008**, *120*, 2926–2929. [\[CrossRef\]](#)
48. Stubenrauch, J.; Broscha, E.; Vohs, J. Reaction of carboxylic acids on CeO₂ (111) and CeO₂ (100). *Catal. Today* **1996**, *28*, 431–441. [\[CrossRef\]](#)
49. Mei, D. First-principles characterization of formate and carboxyl adsorption on stoichiometric CeO₂ (111) and CeO₂ (110) surfaces. *J. Energy Chem.* **2013**, *22*, 524–532. [\[CrossRef\]](#)
50. Senanayake, S.D.; Mullins, D.R. Redox pathways for HCOOH decomposition over CeO₂ surfaces. *J. Phys. Chem. C* **2008**, *112*, 9744–9752. [\[CrossRef\]](#)
51. Zhou, G.; Dai, B.; Xie, H.; Zhang, G.; Xiong, K.; Zheng, X. CeCu composite catalyst for CO synthesis by reverse water–gas shift reaction: Effect of Ce/Cu mole ratio. *J. CO₂ Util.* **2017**, *21*, 292–301. [\[CrossRef\]](#)
52. Reddy, B.M.; Thrimurthulu, G.; Katta, L. Design of efficient CexM1–xO2–δ (M= Zr, Hf, Tb and Pr) nanosized model solid solutions for CO oxidation. *Catal. Lett.* **2011**, *141*, 572–581. [\[CrossRef\]](#)
53. Lu, B.; Kawamoto, K. Preparation of mesoporous CeO₂ and monodispersed NiO particles in CeO₂, and enhanced selectivity of NiO/CeO₂ for reverse water gas shift reaction. *Mater. Res. Bull.* **2014**, *53*, 70–78. [\[CrossRef\]](#)
54. Wang, L.; Liu, H.; Chen, Y.; Yang, S. Reverse water–gas shift reaction over co-precipitated Co–CeO₂ catalysts: Effect of Co content on selectivity and carbon formation. *Int. J. Hydrogen Energy* **2017**, *42*, 3682–3689. [\[CrossRef\]](#)
55. Aitbekova, A.; Wu, L.; Wrasman, C.J.; Boubnov, A.; Hoffman, A.S.; Goodman, E.D.; Bare, S.R.; Cargnello, M. Low-temperature restructuring of CeO₂-supported Ru nanoparticles determines selectivity in CO₂ catalytic reduction. *J. Am. Chem. Soc.* **2018**, *140*, 13736–13745. [\[CrossRef\]](#) [\[PubMed\]](#)

56. Cheng, Z.; Sherman, B.J.; Lo, C.S. Carbon dioxide activation and dissociation on ceria (110): A density functional theory study. *J. Chem. Phys.* **2013**, *138*, 014702. [CrossRef] [PubMed]
57. Lu, X.; Wang, W.; Wei, S.; Guo, C.; Shao, Y.; Zhang, M.; Deng, Z.; Zhu, H.; Guo, W. Initial reduction of CO₂ on perfect and O-defective CeO₂ (111) surfaces: Towards CO or COOH? *RSC Adv.* **2015**, *5*, 97528–97535. [CrossRef]
58. Wu, K.; Sun, L.D.; Yan, C.H. Recent Progress in Well-Controlled Synthesis of Ceria-Based Nanocatalysts towards Enhanced Catalytic Performance. *Adv. Energy Mater.* **2016**, *6*, 1600501. [CrossRef]
59. Trovarelli, A.; Llorca, J. Ceria catalysts at nanoscale: How do crystal shapes shape catalysis? *ACS Catal.* **2017**, *7*, 4716–4735. [CrossRef]
60. Ma, Y.; Gao, W.; Zhang, Z.; Zhang, S.; Tian, Z.; Liu, Y.; Ho, J.C.; Qu, Y. Regulating the surface of nanoceria and its applications in heterogeneous catalysis. *Surf. Sci. Rep.* **2018**, *73*, 1–36. [CrossRef]
61. Saeidi, S.; Najari, S.; Fazlollahi, F.; Nikoo, M.K.; Sefidkon, F.; Klemeš, J.J.; Baxter, L.L. Mechanisms and kinetics of CO₂ hydrogenation to value-added products: A detailed review on current status and future trends. *Renew. Sustain. Energy Rev.* **2017**, *80*, 1292–1311. [CrossRef]
62. Wang, W.; Wang, S.; Ma, X.; Gong, J. Recent advances in catalytic hydrogenation of carbon dioxide. *Chem. Soc. Rev.* **2011**, *40*, 3703–3727. [CrossRef]
63. Porosoff, M.D.; Yan, B.; Chen, J.G. Catalytic reduction of CO₂ by H₂ for synthesis of CO, methanol and hydrocarbons: Challenges and opportunities. *Energy Environ. Sci.* **2016**, *9*, 62–73. [CrossRef]
64. Kattel, S.; Liu, P.; Chen, J.G. Tuning selectivity of CO₂ hydrogenation reactions at the metal/oxide interface. *J. Am. Chem. Soc.* **2017**, *139*, 9739–9754. [CrossRef]
65. Su, X.; Yang, X.; Zhao, B.; Huang, Y. Designing of highly selective and high-temperature durable RWGS heterogeneous catalysts: Recent advances and the future directions. *J. Energy Chem.* **2017**, *26*, 854–867. [CrossRef]
66. Trovarelli, A. *Catalysis by Ceria and Related Materials*; World Scientific: Singapore, 2002; Volume 2.
67. Montini, T.; Melchionna, M.; Monai, M.; Fornasiero, P. Fundamentals and catalytic applications of CeO₂-based materials. *Chem. Rev.* **2016**, *116*, 5987–6041. [CrossRef]
68. Xie, S.; Wang, Z.; Cheng, F.; Zhang, P.; Mai, W.; Tong, Y. Ceria and ceria-based nanostructured materials for photoenergy applications. *Nano Energy* **2017**, *34*, 313–337. [CrossRef]
69. Devaiah, D.; Reddy, L.H.; Park, S.-E.; Reddy, B.M. Ceria–zirconia mixed oxides: Synthetic methods and applications. *Catal. Rev.* **2018**, *60*, 177–277. [CrossRef]
70. Su, X.; Xu, J.; Liang, B.; Duan, H.; Hou, B.; Huang, Y. Catalytic carbon dioxide hydrogenation to methane: A review of recent studies. *J. Energy Chem.* **2016**, *25*, 553–565. [CrossRef]
71. Frontera, P.; Macario, A.; Ferraro, M.; Antonucci, P. Supported catalysts for CO₂ methanation: A review. *Catalysts* **2017**, *7*, 59. [CrossRef]
72. Zhang, M.; Zijlstra, B.; Pilot, I.A.; Li, F.; Wang, H.; Li, J.; Hensen, E.J. A theoretical study of the reverse water-gas shift reaction on Ni (111) and Ni (311) surfaces. *Can. J. Chem. Eng.* **2020**, *98*, 740–748. [CrossRef]
73. Fornero, E.L.; Chiavassa, D.L.; Bonivardi, A.L.; Baltanás, M.A. Transient analysis of the reverse water gas shift reaction on Cu/ZrO₂ and Ga₂O₃/Cu/ZrO₂ catalysts. *J. CO₂ Util.* **2017**, *22*, 289–298. [CrossRef]
74. Zhu, M.; Ge, Q.; Zhu, X. Catalytic reduction of CO₂ to CO via reverse water gas shift reaction: Recent advances in the design of active and selective supported metal catalysts. *Trans. Tianjin Univ.* **2020**, *26*, 172–187. [CrossRef]
75. Lin, W.; Stocker, K.M.; Schatz, G.C. Mechanisms of hydrogen-assisted CO₂ reduction on nickel. *J. Am. Chem. Soc.* **2017**, *139*, 4663–4666. [CrossRef]
76. González-Castaño, M.; Dorneanu, B.; Arellano-García, H. The reverse water gas shift reaction: A process systems engineering perspective. *React. Chem. Eng.* **2021**, *6*, 954–976.
77. Kim, K.-J.; Lee, Y.-L.; Na, H.-S.; Ahn, S.-Y.; Shim, J.-O.; Jeon, B.-H.; Roh, H.-S. Efficient waste to energy conversion based on CO-CeO₂ catalyzed water-gas shift reaction. *Catalysts* **2020**, *10*, 420.
78. Mathew, T.; Saju, S.; Raveendran, S.N. Survey of Heterogeneous Catalysts for the CO₂ Reduction to CO via Reverse Water Gas Shift. In *Engineering Solutions for CO₂ Conversion*; Reina, T.R., Arellano-Garcia, H., Odriozola, J.A., Eds.; Wiley: Hoboken, NJ, USA, 2021; Chapter 12; pp. 281–316.
79. Kim, S.S.; Lee, H.H.; Hong, S.C. A study on the effect of support's reducibility on the reverse water-gas shift reaction over Pt catalysts. *Appl. Catal. A Gen.* **2012**, *423*, 100–107.
80. Wang, L.-C.; Khazaneh, M.T.; Widmann, D.; Behm, R.J. TAP reactor studies of the oxidizing capability of CO₂ on a Au/CeO₂ catalyst—A first step toward identifying a redox mechanism in the Reverse Water–Gas Shift reaction. *J. Catal.* **2013**, *302*, 20–30.
81. Lin, L.; Yao, S.; Liu, Z.; Zhang, F.; Li, N.; Vovchok, D.; Martinez-Arias, A.; Castañeda, R.; Lin, J.; Senanayake, S.D. In situ characterization of Cu/CeO₂ nanocatalysts for CO₂ hydrogenation: Morphological effects of nanostructured ceria on the catalytic activity. *J. Phys. Chem. C* **2018**, *122*, 12934–12943.
82. Lee, S.M.; Eom, H.; Kim, S.S. A study on the effect of CeO₂ addition to a Pt/TiO₂ catalyst on the reverse water gas shift reaction. *Environ. Technol.* **2021**, *42*, 182–192.
83. Liu, Y.; Li, Z.; Xu, H.; Han, Y. Reverse water–gas shift reaction over ceria nanocube synthesized by hydrothermal method. *Catal. Commun.* **2016**, *76*, 1–6.

84. Goguet, A.; Meunier, F.C.; Tibiletti, D.; Breen, J.P.; Burch, R. Spectrokinetic investigation of reverse water-gas-shift reaction intermediates over a Pt/CeO₂ catalyst. *J. Phys. Chem. B* **2004**, *108*, 20240–20246.
85. Zhu, X.; Qu, X.; Li, X.; Liu, J.; Liu, J.; Zhu, B.; Shi, C. Selective reduction of carbon dioxide to carbon monoxide over Au/CeO₂ catalyst and identification of reaction intermediate. *Chin. J. Catal.* **2016**, *37*, 2053–2058.
86. Lu, B.; Zhang, T.; Zhang, L.; Xu, Y.; Zhang, Z.; Wu, F.; Li, X.; Luo, C. Promotion effects of oxygen vacancies on activity of Na-doped CeO₂ catalysts for reverse water gas shift reaction. *Appl. Surf. Sci.* **2022**, *587*, 152881.
87. Wang, M.; Shen, M.; Jin, X.; Tian, J.; Li, M.; Zhou, Y.; Zhang, L.; Li, Y.; Shi, J. Oxygen vacancy generation and stabilization in CeO_{2-x} by Cu introduction with improved CO₂ photocatalytic reduction activity. *ACS Catal.* **2019**, *9*, 4573–4581. [\[CrossRef\]](#)
88. Zhang, Y.; Liang, L.; Chen, Z.; Wen, J.; Zhong, W.; Zou, S.; Fu, M.; Chen, L.; Ye, D. Highly efficient Cu/CeO₂-hollow nanospheres catalyst for the reverse water-gas shift reaction: Investigation on the role of oxygen vacancies through in situ UV-Raman and DRIFTS. *Appl. Surf. Sci.* **2020**, *516*, 146035. [\[CrossRef\]](#)
89. Jacobs, G.; Davis, B.H. Reverse water-gas shift reaction: Steady state isotope switching study of the reverse water-gas shift reaction using in situ DRIFTS and a Pt/ceria catalyst. *Appl. Catal. A Gen.* **2005**, *284*, 31–38. [\[CrossRef\]](#)
90. Dai, H.; Zhang, A.; Xiong, S.; Xiao, X.; Zhou, C.; Pan, Y. The Catalytic Performance of Ga₂O₃–CeO₂ Composite Oxides over Reverse Water Gas Shift Reaction. *ChemCatChem* **2022**, *14*, e202200049. [\[CrossRef\]](#)
91. Li, M.; My Pham, T.H.; Ko, Y.; Zhao, K.; Zhong, L.; Luo, W.; Züttel, A. Support-Dependent Cu–In Bimetallic Catalysts for Tailoring the Activity of Reverse Water Gas Shift Reaction. *ACS Sustain. Chem. Eng.* **2022**, *10*, 1524–1535. [\[CrossRef\]](#)
92. Meunier, F.C.; Tibiletti, D.; Goguet, A.; Reid, D.; Burch, R. On the reactivity of carbonate species on a Pt/CeO₂ catalyst under various reaction atmospheres: Application of the isotopic exchange technique. *Appl. Catal. A Gen.* **2005**, *289*, 104–112. [\[CrossRef\]](#)
93. Kalamaras, C.M.; Americanou, S.; Efstathiou, A.M. “Redox” vs “associative formate with–OH group regeneration” WGS reaction mechanism on Pt/CeO₂: Effect of platinum particle size. *J. Catal.* **2011**, *279*, 287–300. [\[CrossRef\]](#)
94. Chen, X.; Su, X.; Liang, B.; Yang, X.; Ren, X.; Duan, H.; Huang, Y.; Zhang, T. Identification of relevant active sites and a mechanism study for reverse water gas shift reaction over Pt/CeO₂ catalysts. *J. Energy Chem.* **2016**, *25*, 1051–1057. [\[CrossRef\]](#)
95. Juarez, R.; Parker, S.F.; Concepcion, P.; Corma, A.; Garcia, H. Heterolytic and heterotopic dissociation of hydrogen on ceria-supported gold nanoparticles. Combined inelastic neutron scattering and FT-IR spectroscopic study on the nature and reactivity of surface hydrogen species. *Chem. Sci.* **2010**, *1*, 731–738. [\[CrossRef\]](#)
96. Wang, L.; Widmann, D.; Behm, R.J. Reactive removal of surface oxygen by H₂, CO and CO/H₂ on a Au/CeO₂ catalyst and its relevance to the preferential CO oxidation (PROX) and reverse water gas shift (RWGS) reaction. *Catal. Sci. Technol.* **2015**, *5*, 925–941. [\[CrossRef\]](#)
97. Shen, H.; Dong, Y.; Yang, S.; He, Y.; Wang, Q.; Cao, Y.; Wang, W.; Wang, T.; Zhang, Q.; Zhang, H. Identifying the roles of Ce³⁺–OH and Ce–H in the reverse water-gas shift reaction over highly active Ni-doped CeO₂ catalyst. *Nano Res.* **2022**, *15*, 5831–5841. [\[CrossRef\]](#)
98. Deng, B.; Song, H.; Peng, K.; Li, Q.; Ye, J. Metal-organic framework-derived Ga-Cu/CeO₂ catalyst for highly efficient photothermal catalytic CO₂ reduction. *Appl. Catal. B Environ.* **2021**, *298*, 120519. [\[CrossRef\]](#)
99. Zhao, B.; Pan, Y.-X.; Liu, C.-J. The promotion effect of CeO₂ on CO₂ adsorption and hydrogenation over Ga₂O₃. *Catal. Today* **2012**, *194*, 60–64. [\[CrossRef\]](#)
100. Yang, Z.; Zeng, M.; Wang, K.; Yue, X.; Chen, X.; Dai, W.; Fu, X. Visible light-assisted thermal catalytic reverse water gas reaction over Cu-CeO₂: The synergistic of hot electrons and oxygen vacancies induced by LSPR effect. *Fuel* **2022**, *315*, 123186. [\[CrossRef\]](#)
101. Wolf, A.; Jess, A.; Kern, C. Syngas Production via Reverse Water-Gas Shift Reaction over a Ni-Al₂O₃ Catalyst: Catalyst Stability, Reaction Kinetics, and Modeling. *Chem. Eng. Technol.* **2016**, *39*, 1040–1048. [\[CrossRef\]](#)
102. Pekridis, G.; Kalimeri, K.; Kaklidi, N.; Vakouftsi, E.; Iliopoulou, E.; Athanasiou, C.; Marnellos, G. Study of the reverse water gas shift (RWGS) reaction over Pt in a solid oxide fuel cell (SOFC) operating under open and closed-circuit conditions. *Catal. Today* **2007**, *127*, 337–346. [\[CrossRef\]](#)
103. Spencer, M. On the activation energies of the forward and reverse water-gas shift reaction. *Catal. Lett.* **1995**, *32*, 9–13. [\[CrossRef\]](#)
104. Ernst, K.-H.; Campbell, C.T.; Moretti, G. Kinetics of the reverse water-gas shift reaction over Cu (110). *J. Catal.* **1992**, *134*, 66–74. [\[CrossRef\]](#)
105. Ginés, M.; Marchi, A.; Apesteguía, C. Kinetic study of the reverse water-gas shift reaction over CuO/ZnO/Al₂O₃ catalysts. *Appl. Catal. A Gen.* **1997**, *154*, 155–171. [\[CrossRef\]](#)
106. Osaki, T.; Narita, N.; Horiuchi, T.; Sugiyama, T.; Masuda, H.; Suzuki, K. Kinetics of reverse water gas shift (RWGS) reaction on metal disulfide catalysts. *J. Mol. Catal. A Chem.* **1997**, *125*, 63–71. [\[CrossRef\]](#)
107. Poto, S.; van Berkel, D.V.; Gallucci, F.; d’Angelo, M.F.N. Kinetic modelling of the methanol synthesis from CO₂ and H₂ over a CuO/CeO₂/ZrO₂ catalyst: The role of CO₂ and CO hydrogenation. *Chem. Eng. J.* **2022**, *435*, 134946. [\[CrossRef\]](#)
108. Henkel, T. Modellierung Von Reaktion und Stofftransport in Geformten Katalysatoren am Beispiel der Methanolsynthese. Ph.D. Thesis, Technische Universität München, München, Germany, 2011.
109. Graaf, G.; Stamhuis, E.; Beenackers, A. Kinetics of low-pressure methanol synthesis. *Chem. Eng. Sci.* **1988**, *43*, 3185–3195. [\[CrossRef\]](#)
110. Lalinde, J.A.H.; Roongruangsree, P.; Ilseemann, J.; Baeumer, M.; Kopyscinski, J. CO₂ methanation and reverse water gas shift reaction. Kinetic study based on in situ spatially-resolved measurements. *Chem. Eng. J.* **2020**, *390*, 124629. [\[CrossRef\]](#)

111. Kopyscinski, J.; Schildhauer, T.J.; Vogel, F.; Biollaz, S.M.; Wokaun, A. Applying spatially resolved concentration and temperature measurements in a catalytic plate reactor for the kinetic study of CO methanation. *J. Catal.* **2010**, *271*, 262–279. [\[CrossRef\]](#)
112. Daza, Y.A.; Kuhn, J.N. CO₂ conversion by reverse water gas shift catalysis: Comparison of catalysts, mechanisms and their consequences for CO₂ conversion to liquid fuels. *RSC Adv.* **2016**, *6*, 49675–49691. [\[CrossRef\]](#)
113. Campbell, C.T.; Ernst, K.-H. *Forward and Reverse Water—Gas Shift Reactions on Model Copper Catalysts: Kinetics and Elementary Steps*; ACS Publications: Washington, DC, USA, 1992.
114. Kim, S.S.; Lee, H.H.; Hong, S.C. The effect of the morphological characteristics of TiO₂ supports on the reverse water–gas shift reaction over Pt/TiO₂ catalysts. *Appl. Catal. B Environ.* **2012**, *119*, 100–108. [\[CrossRef\]](#)
115. Jadhav, S.G.; Vaidya, P.D.; Bhanage, B.M.; Joshi, J.B. Kinetics of reverse water-gas shift reaction over Pt/Al₂O₃ catalyst. *Can. J. Chem. Eng.* **2016**, *94*, 101–106. [\[CrossRef\]](#)
116. Ghodoosi, F.; Khosravi-Nikou, M.R.; Shariati, A. Mathematical Modeling of Reverse Water-Gas Shift Reaction in a Fixed-Bed Reactor. *Chem. Eng. Technol.* **2017**, *40*, 598–607. [\[CrossRef\]](#)
117. Chen, C.S.; Wu, J.H.; Lai, T.W. Carbon dioxide hydrogenation on Cu nanoparticles. *J. Phys. Chem. C* **2010**, *114*, 15021–15028. [\[CrossRef\]](#)
118. Najari, S.; Gróf, G.; Saeidi, S.; Gallucci, F. Modeling and optimization of hydrogenation of CO₂: Estimation of kinetic parameters via Artificial Bee Colony (ABC) and Differential Evolution (DE) algorithms. *Int. J. Hydrogen Energy* **2019**, *44*, 4630–4649. [\[CrossRef\]](#)
119. Najari, S.; Saeidi, S.; Gróf, G.; Keil, F.J.; Rodrigues, A.E. Kinetic parameters estimation via dragonfly algorithm (DA) and comparison of cylindrical and spherical reactors performance for CO₂ hydrogenation to hydrocarbons. *Energy Convers. Manage.* **2020**, *226*, 113550. [\[CrossRef\]](#)
120. Brübach, L.; Hodonj, D.; Pfeifer, P. Kinetic Analysis of CO₂ Hydrogenation to Long-Chain Hydrocarbons on a Supported Iron Catalyst. *Ind. Eng. Chem. Res.* **2022**, *61*, 1644–1654. [\[CrossRef\]](#)
121. Luhui, W.; Hui, L.; Yuan, L.; Ying, C.; Shuqing, Y. Influence of preparation method on performance of Ni-CeO₂ catalysts for reverse water-gas shift reaction. *J. Rare Earths* **2013**, *31*, 559–564.
122. Li, Y.; Zhang, B.; Tang, X.; Xu, Y.; Shen, W. Hydrogen production from methane decomposition over Ni/CeO₂ catalysts. *Catal. Commun.* **2006**, *7*, 380–386. [\[CrossRef\]](#)
123. Yisup, N.; Cao, Y.; Feng, W.-L.; Dai, W.-L.; Fan, K.-N. Catalytic oxidation of methane over novel Ce–Ni–O mixed oxide catalysts prepared by oxalate gel-coprecipitation. *Catal. Lett.* **2005**, *99*, 207–213. [\[CrossRef\]](#)
124. Huang, Y.; Wang, A.; Li, L.; Wang, X.; Su, D.; Zhang, T. “Ir-in-ceria”: A highly selective catalyst for preferential CO oxidation. *J. Catal.* **2008**, *255*, 144–152. [\[CrossRef\]](#)
125. Li, L.; Song, L.; Wang, H.; Chen, C.; She, Y.; Zhan, Y.; Lin, X.; Zheng, Q. Water-gas shift reaction over CuO/CeO₂ catalysts: Effect of CeO₂ supports previously prepared by precipitation with different precipitants. *Int. J. Hydrogen Energy* **2011**, *36*, 8839–8849. [\[CrossRef\]](#)
126. Yongyi, H.; Qibiao, L.; Yongzhao, W.; Yongxiang, Z. Selective catalytic dehydration of 1, 4-butanediol to 3-buten-1-ol over CeO₂ with different morphology. *Chin. J. Catal.* **2010**, *31*, 619–622.
127. Dong, X.-F.; Zou, H.-B.; Lin, W.-M. Effect of preparation conditions of CuO–CeO₂–ZrO₂ catalyst on CO removal from hydrogen-rich gas. *Int. J. Hydrogen Energy* **2006**, *31*, 2337–2344. [\[CrossRef\]](#)
128. Xue, L.; Zhang, C.; He, H.; Teraoka, Y. Promotion effect of residual K on the decomposition of N₂O over cobalt–cerium mixed oxide catalyst. *Catal. Today* **2007**, *126*, 449–455. [\[CrossRef\]](#)
129. Mei, Y.; Meisheng, C.; Zhang, N.; Zhiqi, L.; Huang, X. Characterization of CeO₂–ZrO₂ mixed oxides prepared by two different co-precipitation methods. *J. Rare Earths* **2013**, *31*, 251–256.
130. Luhui, W.; Hui, L.; Yuan, L.; Ying, C.; Shuqing, Y. Effect of precipitants on Ni-CeO₂ catalysts prepared by a co-precipitation method for the reverse water-gas shift reaction. *J. Rare Earths* **2013**, *31*, 969–974.
131. Dai, B.; Cao, S.; Xie, H.; Zhou, G.; Chen, S. Reduction of CO₂ to CO via reverse water-gas shift reaction over CeO₂ catalyst. *Korean J. Chem. Eng.* **2018**, *35*, 421–427. [\[CrossRef\]](#)
132. Ronda-Lloret, M.; Rico-Francés, S.; Sepúlveda-Escribano, A.; Ramos-Fernandez, E.V. CuOx/CeO₂ catalyst derived from metal organic framework for reverse water-gas shift reaction. *Appl. Catal. A: Gen.* **2018**, *562*, 28–36. [\[CrossRef\]](#)
133. Kim, T.K.; Lee, K.J.; Cheon, J.Y.; Lee, J.H.; Joo, S.H.; Moon, H.R. Nanoporous metal oxides with tunable and nanocrystalline frameworks via conversion of metal–organic frameworks. *J. Am. Chem. Soc.* **2013**, *135*, 8940–8946. [\[CrossRef\]](#)
134. Liu, L.; Fan, F.; Bai, M.; Xue, F.; Ma, X.; Jiang, Z.; Fang, T. Mechanistic study of methanol synthesis from CO₂ hydrogenation on Rh-doped Cu (111) surfaces. *Mol. Catal.* **2019**, *466*, 26–36. [\[CrossRef\]](#)
135. Lykaki, M.; Pachatouridou, E.; Carabineiro, S.A.; Iliopoulou, E.; Andriopoulou, C.; Kallithrakas-Kontos, N.; Boghosian, S.; Konsolakis, M. Ceria nanoparticles shape effects on the structural defects and surface chemistry: Implications in CO oxidation by Cu/CeO₂ catalysts. *Appl. Catal. B: Environ.* **2018**, *230*, 18–28. [\[CrossRef\]](#)
136. Zheng, X.; Li, Y.; Zhang, L.; Shen, L.; Xiao, Y.; Zhang, Y.; Au, C.; Jiang, L. Insight into the effect of morphology on catalytic performance of porous CeO₂ nanocrystals for H₂S selective oxidation. *Appl. Catal. B Environ.* **2019**, *252*, 98–110. [\[CrossRef\]](#)
137. Kovacevic, M.; Mojet, B.L.; van Ommen, J.G.; Lefferts, L. Effects of morphology of cerium oxide catalysts for reverse water gas shift reaction. *Catal. Lett.* **2016**, *146*, 770–777. [\[CrossRef\]](#)
138. Esch, F.; Fabris, S.; Zhou, L.; Montini, T.; Africh, C.; Fornasiero, P.; Comelli, G.; Rosei, R. Electron localization determines defect formation on ceria substrates. *Science* **2005**, *309*, 752–755. [\[CrossRef\]](#)

139. Skorodumova, N.; Baudin, M.; Hermansson, K. Surface properties of CeO₂ from first principles. *Phys. Rev. B* **2004**, *69*, 075401. [\[CrossRef\]](#)
140. Konsolakis, M.; Lykaki, M.; Stefa, S.; Carabineiro, S.A.; Varvoutis, G.; Papista, E.; Marnellos, G.E. CO₂ hydrogenation over nanoceria-supported transition metal catalysts: Role of ceria morphology (nanorods versus nanocubes) and active phase nature (Co versus Cu). *Nanomaterials* **2019**, *9*, 1739. [\[CrossRef\]](#) [\[PubMed\]](#)
141. Kim, M.-S.; Chung, S.-H.; Yoo, C.-J.; Lee, M.S.; Cho, I.-H.; Lee, D.-W.; Lee, K.-Y. Catalytic reduction of nitrate in water over Pd-Cu/TiO₂ catalyst: Effect of the strong metal-support interaction (SMSI) on the catalytic activity. *Appl. Catal. B Environ.* **2013**, *142*, 354–361. [\[CrossRef\]](#)
142. Liotta, L.; Longo, A.; Macaluso, A.; Martorana, A.; Pantaleo, G.; Venezia, A.; Deganello, G. Influence of the SMSI effect on the catalytic activity of a Pt (1%)/Ce_{0.6}Zr_{0.4}O₂ catalyst: SAXS, XRD, XPS and TPR investigations. *Appl. Catal. B Environ.* **2004**, *48*, 133–149. [\[CrossRef\]](#)
143. Bertella, F.; Concepción, P.; Martínez, A. The impact of support surface area on the SMSI decoration effect and catalytic performance for Fischer-Tropsch synthesis of Co-Ru/TiO₂-anatase catalysts. *Catal. Today* **2017**, *296*, 170–180. [\[CrossRef\]](#)
144. Tauster, S.; Fung, S.; Garten, R.L. Strong metal-support interactions. Group 8 noble metals supported on titanium dioxide. *J. Am. Chem. Soc.* **1978**, *100*, 170–175. [\[CrossRef\]](#)
145. Hosokawa, S.; Taniguchi, M.; Utani, K.; Kanai, H.; Imamura, S. Affinity order among noble metals and CeO₂. *Appl. Catal. A: Gen.* **2005**, *289*, 115–120. [\[CrossRef\]](#)
146. Ivanova, A.; Slavinskaya, E.; Gulyaev, R.; Zaikovskii, V.; Stonkus, O.; Danilova, I.; Plyasova, L.; Polukhina, I.; Boronin, A. Metal-support interactions in Pt/Al₂O₃ and Pd/Al₂O₃ catalysts for CO oxidation. *Appl. Catal. B Environ.* **2010**, *97*, 57–71. [\[CrossRef\]](#)
147. Strobel, R.; Pratsinis, S.E. Flame synthesis of supported platinum group metals for catalysis and sensors. *Platin. Met. Rev.* **2009**, *53*, 11–20. [\[CrossRef\]](#)
148. Zou, H.; Dong, X.; Lin, W. Selective CO oxidation in hydrogen-rich gas over CuO/CeO₂ catalysts. *Appl. Surf. Sci.* **2006**, *253*, 2893–2898. [\[CrossRef\]](#)
149. Zhou, G.; Xie, F.; Deng, L.; Zhang, G.; Xie, H. Supported mesoporous Cu/CeO₂- δ catalyst for CO₂ reverse water-gas shift reaction to syngas. *Int. J. Hydrogen Energy* **2020**, *45*, 11380–11393. [\[CrossRef\]](#)
150. Tauster, S. Strong metal-support interactions. *Acc. Chem. Res.* **1987**, *20*, 389–394. [\[CrossRef\]](#)
151. Matte, L.P.; Kilian, A.S.; Luza, L.; Alves, M.C.; Morais, J.; Baptista, D.L.; Dupont, J.; Bernardi, F. Influence of the CeO₂ support on the reduction properties of Cu/CeO₂ and Ni/CeO₂ nanoparticles. *J. Phys. Chem. C* **2015**, *119*, 26459–26470. [\[CrossRef\]](#)
152. Thill, A.S.; Kilian, A.S.; Bernardi, F. Key role played by metallic nanoparticles on the ceria reduction. *J. Phys. Chem. C* **2017**, *121*, 25323–25332. [\[CrossRef\]](#)
153. Figueiredo, W.T.; Escudero, C.; Perez-Dieste, V.; Ospina, C.A.; Bernardi, F. Determining the Surface Atomic Population of Cu_xNi_{1-x}/CeO₂ (0 < x ≤ 1) Nanoparticles during the Reverse Water-Gas Shift (RWGS) Reaction. *J. Phys. Chem. C* **2020**, *124*, 16868–16878.
154. Einakchi, R. Metal Nanoparticles Over Active Ionic-Conductive Supports for the Reverse Water Gas Shift Reaction. Master's Dissertation, Université d'Ottawa/University of Ottawa, Ottawa, ON, Canada, 2016.
155. Wang, L.; Liu, H. Mesoporous Co-CeO₂ catalyst prepared by colloidal solution combustion method for reverse water-gas shift reaction. *Catal. Today* **2018**, *316*, 155–161. [\[CrossRef\]](#)
156. Jurković, D.L.; Pohar, A.; Dasireddy, V.D.; Likozar, B. Effect of copper-based catalyst support on reverse water-gas shift reaction (RWGS) activity for CO₂ reduction. *Chem. Eng. Technol.* **2017**, *40*, 973–980. [\[CrossRef\]](#)
157. Bouarab, R.; Akdim, O.; Aurooux, A.; Cherifi, O.; Mirodatos, C. Effect of MgO additive on catalytic properties of Co/SiO₂ in the dry reforming of methane. *Appl. Catal. A Gen.* **2004**, *264*, 161–168. [\[CrossRef\]](#)
158. Pino, L.; Vita, A.; Cipitì, F.; Laganà, M.; Recupero, V. Hydrogen production by methane tri-reforming process over Ni-ceria catalysts: Effect of La-doping. *Appl. Catal. B Environ.* **2011**, *104*, 64–73. [\[CrossRef\]](#)
159. Chen, X.; Su, X.; Duan, H.; Liang, B.; Huang, Y.; Zhang, T. Catalytic performance of the Pt/TiO₂ catalysts in reverse water gas shift reaction: Controlled product selectivity and a mechanism study. *Catal. Today* **2017**, *281*, 312–318. [\[CrossRef\]](#)
160. Liu, L.; Corma, A. Metal catalysts for heterogeneous catalysis: From single atoms to nanoclusters and nanoparticles. *Chem. Rev.* **2018**, *118*, 4981–5079. [\[CrossRef\]](#) [\[PubMed\]](#)
161. Li, S.; Xu, Y.; Chen, Y.; Li, W.; Lin, L.; Li, M.; Deng, Y.; Wang, X.; Ge, B.; Yang, C. Tuning the selectivity of catalytic carbon dioxide hydrogenation over iridium/cerium oxide catalysts with a strong metal-support interaction. *Angew. Chem.* **2017**, *129*, 10901–10905. [\[CrossRef\]](#)
162. Chen, X.; Chen, Y.; Song, C.; Ji, P.; Wang, N.; Wang, W.; Cui, L. Recent advances in supported metal catalysts and oxide catalysts for the reverse water-gas shift reaction. *Front. Chem.* **2020**, *8*, 709. [\[CrossRef\]](#) [\[PubMed\]](#)
163. Zhao, Z.; Wang, M.; Ma, P.; Zheng, Y.; Chen, J.; Li, H.; Zhang, X.; Zheng, K.; Kuang, Q.; Xie, Z.-X. Atomically dispersed Pt/CeO₂ catalyst with superior CO selectivity in reverse water gas shift reaction. *Appl. Catal. B Environ.* **2021**, *291*, 120101. [\[CrossRef\]](#)
164. Wang, W.; Zhang, Y.; Wang, Z.; Yan, J.-M.; Ge, Q.; Liu, C.-J. Reverse water gas shift over In₂O₃-CeO₂ catalysts. *Catal. Today* **2016**, *259*, 402–408. [\[CrossRef\]](#)

165. Ro, I.; Sener, C.; Stadelman, T.M.; Ball, M.R.; Venegas, J.M.; Burt, S.P.; Hermans, I.; Dumesic, J.A.; Huber, G.W. Measurement of intrinsic catalytic activity of Pt monometallic and Pt-MoOx interfacial sites over visible light enhanced PtMoOx/SiO₂ catalyst in reverse water gas shift reaction. *J. Catal.* **2016**, *344*, 784–794. [\[CrossRef\]](#)
166. Pettigrew, D.; Trimm, D.; Cant, N. The effects of rare earth oxides on the reverse water-gas shift reaction on palladium/alumina. *Catal. Lett.* **1994**, *28*, 313–319. [\[CrossRef\]](#)
167. Yang, L.; Pastor-Pérez, L.; Gu, S.; Sepúlveda-Escribano, A.; Reina, T. Highly efficient Ni/CeO₂-Al₂O₃ catalysts for CO₂ upgrading via reverse water-gas shift: Effect of selected transition metal promoters. *Appl. Catal. B Environ.* **2018**, *232*, 464–471. [\[CrossRef\]](#)
168. Dorner, R.W.; Hardy, D.R.; Williams, F.W.; Willauer, H.D. Effects of ceria-doping on a CO₂ hydrogenation iron-manganese catalyst. *Catal. Commun.* **2010**, *11*, 816–819. [\[CrossRef\]](#)
169. Galvita, V.V.; Poelman, H.; Bliznuk, V.; Detavernier, C.; Marin, G.B. CeO₂-modified Fe₂O₃ for CO₂ utilization via chemical looping. *Ind. Eng. Chem. Res.* **2013**, *52*, 8416–8426. [\[CrossRef\]](#)
170. Yan, B.; Zhao, B.; Kattel, S.; Wu, Q.; Yao, S.; Su, D.; Chen, J.G. Tuning CO₂ hydrogenation selectivity via metal-oxide interfacial sites. *J. Catal.* **2019**, *374*, 60–71. [\[CrossRef\]](#)
171. Rahmani, F.; Haghighi, M.; Estifae, P. Synthesis and characterization of Pt/Al₂O₃-CeO₂ nanocatalyst used for toluene abatement from waste gas streams at low temperature: Conventional vs. plasma-ultrasound hybrid synthesis methods. *Microporous Mesoporous Mater.* **2014**, *185*, 213–223. [\[CrossRef\]](#)
172. Zonetti, P.C.; Letichevsky, S.; Gaspar, A.B.; Sousa-Aguiar, E.F.; Appel, L.G. The Ni_xCe_{0.75}Zr_{0.25-x}O₂ solid solution and the RWGS. *Appl. Catal. A Gen.* **2014**, *475*, 48–54. [\[CrossRef\]](#)
173. Wenzel, M.; Rihko-Struckmann, L.; Sundmacher, K. Continuous production of CO from CO₂ by RWGS chemical looping in fixed and fluidized bed reactors. *Chem. Eng. J.* **2018**, *336*, 278–296. [\[CrossRef\]](#)
174. Yang, L.; Pastor-Pérez, L.; Villora-Picó, J.J.; Gu, S.; Sepúlveda-Escribano, A.; Reina, T.R. CO₂ valorisation via reverse water-gas shift reaction using promoted Fe/CeO₂-Al₂O₃ catalysts: Showcasing the potential of advanced catalysts to explore new processes design. *Appl. Catal. A Gen.* **2020**, *593*, 117442. [\[CrossRef\]](#)
175. Ray, K.; Sengupta, S.; Deo, G. Reforming and cracking of CH₄ over Al₂O₃ supported Ni, Ni-Fe and Ni-Co catalysts. *Fuel Process. Technol.* **2017**, *156*, 195–203. [\[CrossRef\]](#)
176. Theofanidis, S.A.; Galvita, V.V.; Poelman, H.; Marin, G.B. Enhanced carbon-resistant dry reforming Fe-Ni catalyst: Role of Fe. *ACS Catal.* **2015**, *5*, 3028–3039. [\[CrossRef\]](#)
177. Chen, L.; Wu, D.; Wang, C.; Ji, M.; Wu, Z. Study on Cu-Fe/CeO₂ bimetallic catalyst for reverse water gas shift reaction. *J. Environ. Chem. Eng.* **2021**, *9*, 105183. [\[CrossRef\]](#)
178. Goguet, A.; Meunier, F.; Breen, J.; Burch, R.; Petch, M.; Ghenciu, A.F. Study of the origin of the deactivation of a Pt/CeO₂ catalyst during reverse water gas shift (RWGS) reaction. *J. Catal.* **2004**, *226*, 382–392. [\[CrossRef\]](#)
179. Kattel, S.; Yu, W.; Yang, X.; Yan, B.; Huang, Y.; Wan, W.; Liu, P.; Chen, J.G. CO₂ Hydrogenation over Oxide-Supported PtCo Catalysts: The Role of the Oxide Support in Determining the Product Selectivity. *Angew. Chem. Int. Ed.* **2016**, *55*, 7968–7973. [\[CrossRef\]](#)
180. Panaritis, C.; Edake, M.; Couillard, M.; Einakchi, R.; Baranova, E.A. Insight towards the role of ceria-based supports for reverse water gas shift reaction over RuFe nanoparticles. *J. CO₂ Util.* **2018**, *26*, 350–358. [\[CrossRef\]](#)
181. Le Saché, E.; Pastor-Pérez, L.; Haycock, B.J.; Villora-Picó, J.J.; Sepúlveda-Escribano, A.; Reina, T.R. Switchable catalysts for chemical CO₂ recycling: A step forward in the methanation and reverse water-Gas shift reactions. *ACS Sustain. Chem. Eng.* **2020**, *8*, 4614–4622. [\[CrossRef\]](#)
182. Choi, E.J.; Lee, Y.H.; Lee, D.-W.; Moon, D.-J.; Lee, K.-Y. Hydrogenation of CO₂ to methanol over Pd-Cu/CeO₂ catalysts. *Mol. Catal.* **2017**, *434*, 146–153. [\[CrossRef\]](#)
183. Porosoff, M.D.; Yang, X.; Boscoboinik, J.A.; Chen, J.G. Molybdenum carbide as alternative catalysts to precious metals for highly selective reduction of CO₂ to CO. *Angew. Chem. Int. Ed.* **2014**, *53*, 6705–6709. [\[CrossRef\]](#) [\[PubMed\]](#)
184. Yang, S.-C.; Pang, S.H.; Sulmonetti, T.P.; Su, W.-N.; Lee, J.-F.; Hwang, B.-J.; Jones, C.W. Synergy between ceria oxygen vacancies and Cu nanoparticles facilitates the catalytic conversion of CO₂ to CO under mild conditions. *ACS Catal.* **2018**, *8*, 12056–12066. [\[CrossRef\]](#)
185. Dai, B.; Zhou, G.; Ge, S.; Xie, H.; Jiao, Z.; Zhang, G.; Xiong, K. CO₂ reverse water-gas shift reaction on mesoporous M-CeO₂ catalysts. *Can. J. Chem. Eng.* **2017**, *95*, 634–642. [\[CrossRef\]](#)
186. Vovchok, D.; Zhang, C.; Hwang, S.; Jiao, L.; Zhang, F.; Liu, Z.; Senanayake, S.D.; Rodriguez, J.A. Deciphering dynamic structural and mechanistic complexity in Cu/CeO₂/ZSM-5 catalysts for the reverse water-gas shift reaction. *ACS Catal.* **2020**, *10*, 10216–10228. [\[CrossRef\]](#)
187. Wang, L.; Liu, H.; Chen, Y.; Zhang, R.; Yang, S. K-Promoted Co-CeO₂ Catalyst for the Reverse Water-Gas Shift Reaction. *Chem. Lett.* **2013**, *42*, 682–683. [\[CrossRef\]](#)
188. Luhui, W.; Zhang, S.; Yuan, L. Reverse water gas shift reaction over Co-precipitated Ni-CeO₂ catalysts. *J. Rare Earths* **2008**, *26*, 66–70.
189. Sun, F.-M.; Yan, C.-F.; Guo, C.-Q.; Huang, S.-L. Ni/Ce-Zr-O catalyst for high CO₂ conversion during reverse water gas shift reaction (RWGS). *Int. J. Hydrogen Energy* **2015**, *40*, 15985–15993. [\[CrossRef\]](#)
190. Belekar, R. Suppression of coke formation during reverse water-gas shift reaction for CO₂ conversion using highly active Ni/Al₂O₃-CeO₂ catalyst material. *Phys. Lett. A* **2021**, *395*, 127206. [\[CrossRef\]](#)